A new grid of synthetic spectra for the analysis of [WC]-type central stars of planetary nebulae

Graziela R. Keller,[1,2]⋆ James E. Herald,[2] Luciana Bianchi,[2] Walter J. Maciel[1] and Ralph C. Bohlin[3]

[1]*Instituto de Astronomia, Geofísica e Ciências Atmosféricas, Universidade de São Paulo, Cidade Universitária, São Paulo/SP, Brazil*
[2]*Department of Physics and Astronomy, The Johns Hopkins University, 3400 N. Charles Street, Baltimore, MD 21218, USA*
[3]*Space Telescope Science Institute, 3700 San Martin Drive, Baltimore, MD 21218, USA*

ABSTRACT

We present a comprehensive grid of synthetic stellar-atmosphere spectra, suitable for the analysis of high-resolution spectra of hydrogen-deficient post-asymptotic giant branch objects hotter than 50 000 K, migrating along the constant luminosity branch of the Hertzsprung–Russell diagram. The grid was calculated with CMFGEN, a state-of-the-art stellar atmosphere code that properly treats the stellar winds, accounting for expanding atmospheres in non-local thermodynamic equilibrium, line blanketing, soft X-rays and wind clumping. We include many ionic species that have been previously neglected. Our uniform set of models fills a niche in an important parameter regime, that is, high effective temperatures, high surface gravities and a range of mass-loss values. The grid constitutes a general tool to facilitate determination of the stellar parameters and line identifications and to interpret morphological changes in the stellar spectrum as stars evolve through the central star of planetary nebula phase. We show the effect of major physical parameters on spectral lines in the far-ultraviolet (far-UV), UV and optical regimes. We analyse UV and far-UV spectra of the central star of NGC 6905 using the grid to constrain its physical parameters, and proceed to further explore other parameters not taken into consideration in the grid. This application shows that the grid can be used to constrain the main photospheric and wind parameters, as a first step towards a detailed analysis. The full grid of synthetic spectra, comprising of far-UV, UV, optical and infrared spectral regions, is available online.

Key words: stars: AGB and post-AGB – stars: atmospheres – stars: individual: NGC 6905 – stars: low-mass – stars: mass-loss – stars: winds, outflows.

1 INTRODUCTION

Evolutionary models predict that low- and intermediate-mass stars (of initial masses between 1 and 8 M$_\odot$) leave the asymptotic giant branch (AGB) and evolve through the constant luminosity track of the Hertzsprung–Russell diagram (HRD) up to very high effective temperatures [∼200 000 K, for central stars of planetary nebulae (CSPNe) of about 0.6 M$_\odot$], then turn on to the white dwarf (WD) cooling track, where their luminosities fade while their effective temperatures decrease and, finally, they end their lives as WDs (see e.g. Vassiliadis & Wood 1994; Herwig 2005, and references therein). As the post-AGB stars evolve towards higher temperatures, they ionize the surrounding hydrogen-rich material previously ejected by the AGB precursors, giving rise to bright PNe. Because these

objects expel the majority of their initial mass prior to settling on the WD cooling sequence, they are a prime source of chemically processed material for the interstellar medium (ISM) and thus a fundamental ingredient of galactic chemical evolution (e.g. Marigo 2001; Bianchi et al. 2011a; Karakas 2010, and references therein). In addition, their intense ultraviolet (UV) radiation fields and fast winds during the post-AGB phase can influence the dynamics of the ISM.

Approximately 20 per cent of the CSPNe are hydrogen deficient, a condition thought to be due to thermal pulses that occur after the star leaves the AGB. These pulses can happen at different epochs of the evolution, resulting in stars with different properties. If the thermal pulse occurs after the star has already entered the WD cooling track, it is termed a very late thermal pulse (VLTP) (from the 'born-again' scenario of Iben et al. 1983). The late thermal pulse (LTP) occurs during the CSPN phase while hydrogen burning is still ongoing. In both cases, the star returns towards the AGB. The star can also

⋆E-mail: graziela@astro.iag.usp.br

undergo an AGB final thermal pulse or AFTP , which happens at the end of the AGB phase (Blöcker 2001; Herwig 2001). The amount of the remaining hydrogen varies among these scenarios. A VLTP produces hydrogen-free stars (Werner & Herwig 2006), while in the LTP case, the hydrogen content at the star surface is decreased to a few per cent by mass. If the star undergoes an AFTP instead, it is left with a relatively high hydrogen content. A measurement of the nitrogen abundance can help distinguish whether a VLTP or a LTP has occurred, because the evolution of the stellar nitrogen content is different in each of these scenarios, resulting in an abundance of about 0.1 per cent by mass in the case of a LTP event and up to a few per cent in the case of a VLTP event (Werner et al. 2006). The three scenarios also predict somewhat different helium, carbon and oxygen abundances; therefore, measurements of these quantities help to determine if the star underwent a LTP, VLTP or AFTP event (see e.g. Blöcker 2001, and references therein).

The H-deficient CSPNe are commonly divided into three main classes, which are thought to constitute an evolutionary sequence. These are [WC], showing spectra very similar to those of Population I Wolf–Rayet (WR) stars, with strong carbon and helium emission lines; the PG1159 type, occupying the region at the top of the WD cooling track in the HRD and characterized by absorption lines of highly ionized He, C and O, besides UV wind lines much weaker than the ones seen in [WC] stars; and [WC]-PG1159, that are believed to be transition objects between the two other classes. The [WC] stars are further divided into early ([WCE]) and late-type ([WCL]) objects, showing lines from ions of higher and lower ionization stages, respectively. The evolution of the H-deficient CSPNe might proceed in the following way: AGB → [WCL] → [WCE] → [WC]-PG1159 → PG1159 → WD (Werner & Heber 1991; Górny & Tylenda 2000; Peña, Stasińska & Medina 2001). According to this scenario, the [WC] CSPNe would evolve from the AGB at an almost constant luminosity, towards higher temperatures. As the stars evolve, their radii decrease until the nuclear burning ceases and the stars progress quickly as PG1159 on to the WD cooling track, while luminosity and mass-loss decrease and the wind reaches very high terminal velocities.

A solid determination of the photospheric and wind parameters, as well as of the chemical composition of CSPNe, is crucial to address questions concerning the stellar evolution, the connection between the classes of H-deficient central stars, the wind-driving mechanism and its effect on the ISM, and to understand the surrounding nebulae. Modelling the observed spectrum with stellar atmosphere codes is the most direct method for the derivation of stellar parameters, and constructing model grids covering the relevant range of parameters is the best way to accomplish a systematic analysis, and constrain the major parameters.

The majority of CSPN spectral analyses in the past have been carried out in an ad hoc fashion, that is, sets of models being calculated for each observed CSPN. These models vary in sophistication, with more or less ions being included in the calculations, allowing or not for wind clumping, etc. (see e.g. Leuenhagen, Hamann & Jeffery 1996; Koesterke & Hamann 1997b; Koesterke, Dreizler & Rauch 1998; Leuenhagen & Hamann 1998; De Marco et al. 2001; Herald & Bianchi 2004a; Herald, Bianchi & Hillier 2005; Marcolino et al. 2007). To date, only a few Galactic CSPNe are well studied. With the *GALEX* surveys (Martin et al. 2005; Bianchi 2009), thousands of Milky Way post-AGB objects, including CSPNe and WDs, are being measured photometrically in the UV (Bianchi et al. 2005, 2007b, 2011a,b). Therefore, a general tool to facilitate determination of the stellar parameters will allow researchers to exploit the many-fold increase in samples of these objects and to finally clarify

the final stages of stellar evolution. We constructed a large grid of models covering the CSPN parameter space, which can be used to quickly constrain the main parameters and limit the need of 'ad hoc' computed models in each case.

Several grids of stellar atmosphere models have been calculated to help analyse data for massive early-type stars. Examples include for main-sequence, giants and supergiant stars, the 'Kurucz' [in local thermodynamic equilibrium (LTE) and hydrostatic equilibrium] models (Kurucz 1991); for WN WR stars, the non-LTE grids of Hamann & Gräfener (2004), which account for winds; for O stars, the non-LTE, hydrostatic equilibrium TLUSTY OSTAR 2002 models (Lanz & Hubeny 2003) and the non-LTE, accounting for expanding atmospheres, WM-basic grids of Bianchi & Garcia (in preparation) and, in a more limited fashion, Pauldrach, Hoffmann & Lennon (2001); for B stars, the non-LTE, hydrostatic equilibrium TLUSTY BSTAR 2006 models (Lanz & Hubeny 2007). For CSPNe, Clegg & Middlemass (1987) computed a grid of non-LTE, plane-parallel model atmospheres, in hydrostatic equilibrium, with H and He opacity sources. Also, Rauch (2003) presented a grid of non-LTE, plane-parallel, line-blanketed models calculated in hydrostatic equilibrium, useful for the analysis of H-rich CSPNe and their PNe. Only relatively recent advances in both computing power and stellar atmosphere codes made it possible to generate models that adequately reproduce most of the wind features in the spectra of CSPNe with winds. As a consequence, grids of non-LTE models, accounting for line-blanketed expanding atmospheres and clumping, spanning this important phase of post-AGB evolution do not yet exist. The grid presented here is the first step towards filling this gap.

In this paper, we present a grid of synthetic spectra for the analysis of spectroscopic data from [WC] CSPNe hotter than 50 000 K. This paper is organized as follows. Section 2 describes the stellar atmosphere code. We describe the grid in Section 3 and present illustrative results in Section 4. In Section 5, we apply the grid to derive physical parameters of NGC 6905 in order to illustrate the use of the model grid. This paper finishes with conclusions in Section 6.

2 THE CODE

[WC]-type CSPNe are very hot, with temperatures ranging from ∼20 000 to 200 000 K and extended atmospheres, which expand reaching supersonic velocities. Line blanketing affects their atmospheric structure and emergent spectra. Not all CSPNe have dense winds, since the presence of intense mass-loss, if driven by radiation pressure, is related to the closeness of the star to the Eddington limit (Pauldrach et al. 1988). For example, as the PG1159 central stars approach the WD cooling track, their winds fade and their spectral lines are less and less conspicuous (see examples in Werner, Rauch & Kruk 2010). The winds of CSPNe are believed to be radiatively driven and as such subjected to instabilities, which are theoretically predicted to lead to the formation of clumping and shocks emitting soft X-rays (Owocki, Castor & Rybicki 1988). Such effects were quantified observationally in the winds of massive O-type stars (Bianchi & Garcia 2002; Garcia & Bianchi 2004; Bianchi, Herald & Garcia 2009). The grid of models was calculated using the non-LTE radiative transfer code CMFGEN (Hillier & Miller 1998; Herald et al. 2005), which solves iteratively for the level populations and radiation field, assuming radiative equilibrium, in a spherically symmetric expanding outflow. It accounts for wind clumping, soft X-rays and line blanketing through a 'superlevel' approach. CMFGEN was originally developed to model the winds of massive WR stars

and has been adapted for objects with weaker winds such as O-type stars and CSPNe (as described by Hillier et al. 2003; Herald et al. 2005). Details about the code are given in the references above. Here, we briefly describe the more important aspects.

The radiative luminosity is taken to be constant throughout the wind and is given by

$$L = 4\pi R_*^2 \sigma T_*^4, \tag{1}$$

where R_* and T_* are defined at a Rosseland mean optical depth of 20.

CMFGEN does not solve the dynamical equations of the wind, requiring the mass-loss rate and the velocity law to be supplied. Here, we have adopted a standard velocity law, where

$$v(r) = v_\infty \left(1 - \frac{r_0}{r}\right)^\beta, \tag{2}$$

with $\beta = 1$ which is the value usually adopted in modelling these objects. r_0 is roughly equal to R_*.

Currently, CMFGEN requires the density structure to be given. The procedure adopted here was to attach the wind velocity law to the underlying hydrostatic structure of the star (as described in Hillier & Lanz 2001), which we obtain using the TLUSTY code (Hubeny & Lanz 1995). TLUSTY computes plane-parallel, non-LTE atmospheres in hydrostatic equilibrium and requires surface gravity, temperature and abundances as inputs.

Instabilities in the stellar winds of hot stars are thought to generate density inhomogeneities, stochastically distributed throughout the wind, which are usually referred to as clumping (see e.g. Moffat 2008). In CMFGEN, the radiative transfer in an inhomogeneous medium is implemented assuming that the clumps are small compared to the mean free path of the photons and that the interclumping medium is void (this treatment of clumping is sometimes referred to as microclumping approximation). The degree of clumping in the wind is parametrized by the clumping filling factor f, with the density inside the clumps being a factor f^{-1} higher than the density of the homogeneous wind model with the same mass-loss rate. Since, according to this approximation, there is no material in between the clumps, the statistical equations are solved for the intraclump medium. From the ion-level populations obtained, the non-LTE opacities and emissivities for the clump material are calculated. The transfer equation is then solved substituting the homogeneous-wind opacities and emissivities with the ones calculated for the intraclump material multiplied by the filling factor.

The main effect of treating clumps in the above approximation is that it reduces the empirical mass-loss rate by a factor $\sqrt{f^{-1}}$ when using diagnostics that depend on the square of the density, such as emission lines and radio thermal emission. There is evidence of the clumping in the winds of [WC] stars, but the quantification of the clumping factor and its radial variation is made difficult by the weaker electron-scattering wings of intense emission lines of these stars in comparison with their massive WR star counterparts. Despite that, Todt, Hamann & Gräfener (2008), based on the electron-scattering wings of emission lines of three early-type [WC] stars, NGC 6751, 5189 and 1501, found evidence for clumping with $f > 0.25$. Further evidence for the presence of inhomogeneities in these winds comes from the work of Grosdidier, Acker & Moffat (2000, 2001), who interpreted moving features seen on the top of emission lines of the [WC] stars NGC 40 and BD +30 3639 as larger scale outflowing blobs. CMFGEN accounts for clumping using an exponential law,

$$f(v) = f_\infty + (1 - f_\infty) \exp\left[-v(r)/v_{clump}\right], \tag{3}$$

in which the radiative instabilities are supposed to be damped at low wind velocities and, as a consequence, the wind is assumed smooth until a certain wind velocity, v_{clump}, is achieved. Beyond this velocity, the degree of clumping increases outwards until the clumping filling factor finally reaches its terminal value, f_∞, which, in this work, is assumed to be 0.1. In equation (3), $f(v)$ and $v(r)$ are the clumping filling factor and the velocity of the wind at a given radius, respectively. Here, v_{clump} was taken to be 200 km s^{-1}.

CMFGEN accounts for line blanketing, which alters the ionization and temperature structure of the model atmosphere. In particular, the opacity by, for example, iron lines, redistributes the UV radiation field. Neglecting it would lead to an overestimation of the ionization of the atmosphere. The back warming and surface-cooling effects of the line blanketing allow lower ions in the outer layers to co-exist with the higher ones from the deeper layers. Inclusion, in the models, of this phenomenon was noted to better reproduce the spectra of massive WR stars (Hamann & Gräfener 2004). In CMFGEN, the inclusion of the line blanketing is done through the superlevel approximation, in which several energy levels are grouped into a smaller number of superlevels and all the levels within a superlevel share the same departure coefficient.

CMFGEN can also include, in the ionization calculations, the effect of soft X-rays, which would be created in shocks distributed throughout the wind. These shocks are believed to originate from the instability of the line-driving mechanism. X-rays may considerably alter the ionization structure in the atmosphere, since they produce higher ionization stages of certain ions as, for example, O VI and N V (see e.g. Bianchi & Garcia 2002; Garcia & Bianchi 2004; Martins et al. 2005; Bianchi et al. 2007a, and references therein). In CMFGEN, the X-rays are taken into consideration in the calculations, by specifying the temperature and velocity of the shocks. Also, a volume-filling factor for the distribution of X-ray sources has to be given in order to set the level of the emission. The X-ray emissivity is taken from the X-ray code of Raymond & Smith (1977), which at present is available only for solar abundances. In Section 4.4, we describe the effect on the model spectra of including soft X-rays in the calculations.

In order to calculate the detailed emerging spectra, we adopted a microturbulence velocity which varies with depth such that

$$v_{turb}(r) = v_{min} + (v_{max} - v_{min})\frac{v(r)}{v_\infty}, \tag{4}$$

where v_{min} and v_{max} are the minimum and maximum microturbulence velocities, respectively. We assumed $v_{min} = 10$ km s^{-1} and $v_{max} = 50$ km s^{-1} for all the models. The models resolution varies across the wavelength range, with lines being better sampled than continuum regions. As an example, in the model B150.M70.V2500 (see Table 2), the central regions of the emission components of the O VI $\lambda\lambda 1031.9$, 1037.6 Å and C IV $\lambda\lambda 1548.2$, 1550.8 Å lines are sampled by 81 and 46 flux points in a 1 Å interval, respectively.

3 THE GRID

The grid presented here is intended to comprehensively cover the parameter space of [WC] CSPNe. The combination of parameters chosen for each of the grid models approximately follows the evolutionary calculations of Miller Bertolami & Althaus (2006) for CSPNe with the final masses of 0.5, 0.6 and 0.9 M$_\odot$ (which correspond to the initial masses of 1.0, 3.1, and 5.5 M$_\odot$, respectively), as shown in Fig. 1. The stellar parameters L, R_*, T_*, log g and M_* of the grid models are inside the range of values predicted for these stars. A chosen model temperature corresponds to a different model
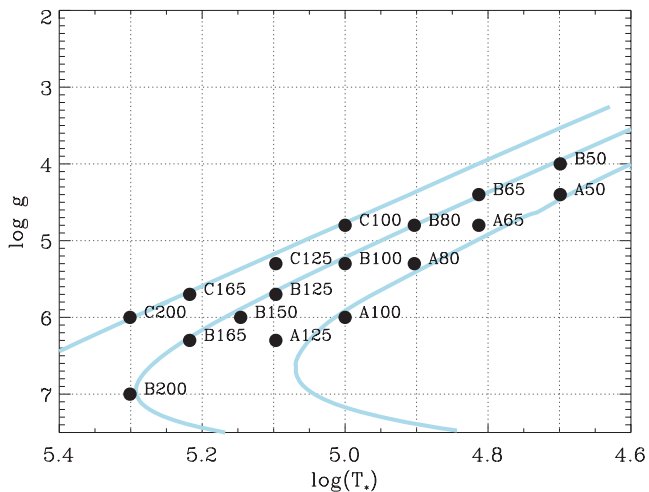
Figure 1. Grid points in the $\log T_*$–$\log g$ plane. The evolutionary tracks of Miller Bertolami & Althaus (2006) are also shown (continuous lines) for CSPNe with 0.5, 0.6 and $0.9 \, M_\odot$, from the right-hand to left-hand side. Each point shown is identified by a label which corresponds to a group of models with the same temperature, surface gravity and radius, but with a range of mass-loss rates and wind's terminal velocities, as can be seen in Tables 1–3.

radius for each of the evolutionary tracks used, since the luminosity varies with mass on the constant luminosity track in the HRD. Also, for the models within one track, each temperature corresponds to a different radius in order to keep an almost constant luminosity.

We have selected eight stellar temperature values ranging from 50 000 to 200 000 K and eight values of $\log g$ between 4.0 and 7.0. For each combination of $\log g$ and T_* seen in Fig. 1, models with different mass-loss rates and wind's terminal velocities were computed. The wind's terminal velocities and the mass-loss rates were chosen to cover the typical values of these parameters found in the literature, taking into account that our models assume a clumped wind, whereas some mass-loss rates were derived in the literature assuming a smooth wind. Additional models differing only in neon abundance were also computed (discussed in Section 4.3). The grid adds up to a total of 199 models. The list of models is given in Tables 1–3. The grid is available online at http://dolomiti.pha.jhu.edu/planetarynebulae.html. There the user will have access to the synthetic spectra and related documentation, along with plots comparing the different models such as shown in Fig. 2.

By following three tracks for different stellar mass values, we covered different combinations of temperature and surface gravity/stellar radius. The [WC] CSPNe with temperatures above 50 000 K are characterized by the lack of strong absorption lines not affected by wind emission, which prevents the determination of their surface gravity through spectral analysis. When the distance is known, the derived stellar parameters can place the object on a specific evolutionary track, from which $\log g$ can be inferred. Otherwise, the analysis can only constrain the transformed radius, and mass and $\log g$ are not uniquely constrained. The transformed radius is defined as

$$R_t = R_* \left(\frac{v_\infty / 2500 \, \text{km s}^{-1}}{\dot{M} / 10^{-4} \, M_\odot \, \text{yr}^{-1}} \right)^{2/3}, \tag{5}$$

and is a measure of how dense the wind is (smaller values of R_t translate into denser winds). Models with the same temperature, differing only in the mass-loss rate and in the stellar radius, but with

the same transformed radius and the same wind's terminal velocity, are known to produce very similar wind features in the UV range (Schmutz, Hamann & Wessolowski 1989; Hamann, Koesterke & Wessolowski 1993).

Models having the same temperature, mass-loss rate and wind's terminal velocity, but from different mass tracks, differ in luminosity, radius, $\log g$ and transformed radius. Different $\log g$ result in differences on the photospheric lines. Differing R_t affect the wind lines. Fig. 3 shows models A100.M67.V2000, B100.M67.V2000 and C100.M67.V2000 that, despite having the same mass-loss and wind's terminal velocity, have very different wind features as a result of their different transformed radii. These three models also differ in $\log g$, but the lack of spectral features free from wind effects makes it impossible to distinguish between different $\log g$ values. Surface gravity, however, influences the emission-line profiles by affecting the underlying photospheric ones.

It is believed that [WCL] and [WCE] stars form an evolutionary sequence due to their locations in the $\log T_{\text{eff}}$–$\log g$ diagram. Carbon and helium are the main constituents of their atmospheres. Spectral analyses have, however, suggested different C:He ratios between the two subtypes (Koesterke & Hamann 1997a,b). De Marco et al. (2001), Crowther et al. (2003) and Marcolino et al. (2007), on the other hand, find no systematic discrepancies in the C:He ratios between [WCL] and [WCE] stars. Thus, since it is not yet clear if the two groups of [WC] CSPNe have different carbon and helium abundance patterns, we adopted a constant C:He ratio for all the models in the grid. Typical measured values for elemental abundances are (by mass): $X_{\text{He}} = 0.33$–0.80, $X_C = 0.15$–0.50 and $X_O = 0.06$–0.17 (Werner 2001). Here, we adopted a C:He ratio of 0.45:0.43 and an oxygen abundance of $X_O = 0.08$ by mass. Nitrogen abundances in these objects typically range from undetectable to ∼2 per cent by mass, and we have adopted $X_N = 0.01$ (Koesterke & Hamann 1997b; Leuenhagen & Hamann 1998). We assumed a neon abundance of 2 per cent by mass, that is, higher than the solar value by a factor of 11.5, since strong overabundances of this order have been reported for [WC] stars (Leuenhagen & Hamann 1998; Herald et al. 2005). Iron is expected to be depleted through the s-process (Herwig, Lugaro & Werner 2003), as was indeed observed by Stasińska et al. (2004). Thus, the grid models have an iron abundance a factor of 100 lower than the solar value. Solar abundances were adopted for all other elements present in the models.

The model calculations include many ionic species that have been previously neglected. The elements and ionic species considered in each model of the grid, along with the number of levels and superlevels used, can be found in the online documentation. The ionic species included in each model vary, since in many cases their number was limited to keep the models within a workable size, or due to the unavailability of precise atomic data. The hotter models were calculated first and, as the temperature was decreased for the calculation of the cooler models, ionic species were introduced as needed based on the analysis of the ionization fractions. Table 4 shows the species considered in the calculation of the grid models.

As a general rule, we considered it not necessary to include a lower ionization stage when the ionization fraction of the lowest included ionization stage was $\leq 10^{-2}$. Tests were performed on representative models in order to assess the necessity of including lower ionization stages. As an example of the procedure, we give here more details about the C III, C IV and C V ions. All models with temperatures up to 80 000 K include C III. For temperatures of the order of 125 000 K, C IV is much less abundant than C V; the bottom panel of Fig. 8 (shown later) illustrates the typical behaviour. For some $T_* = 125\,000$ K models showing relevant C IV ionization

Table 1. Track A stellar parameters of the grid models for CSPNe with $0.5\,M_{\odot}$.

Model	T_* (kK)	$\log(g)$	R_* ($R_{\odot}$)	L_* ($10^3 L_{\odot}$)	$\log(\dot{M})$ ($M_{\odot}\,yr^{-1}$)	v_{∞} (km s^{-1})	R_t ($R_{\odot}$)
A50.M73.V500	50	4.4	0.75	3.1	−7.3	500	40.35
A50.M73.V1000						1000	64.04
A50.M67.V500					−6.7	500	16.02
A50.M67.V1000						1000	25.42
A50.M63.V500					−6.3	500	8.70
A50.M63.V1000						1000	13.80
A65.M73.V500	65	4.8	0.47	3.5	−7.3	500	25.55
A65.M73.V1000						1000	40.56
A65.M67.V500					−6.7	500	10.14
A65.M67.V1000						1000	16.10
A65.M63.V500					−6.3	500	5.51
A65.M63.V1000						1000	8.74
A80.M73.V500	80	5.3	0.27	2.5	−7.3	500	14.36
A80.M73.V1000						1000	22.80
A80.M67.V500					−6.7	500	5.70
A80.M67.V1000						1000	9.05
A80.M63.V500					−6.3	500	3.10
A80.M63.V1000						1000	4.91
A100.M73.V1500	100	6.0	0.12	1.2	−7.3	1500	13.30
A100.M73.V2000						2000	16.12
A100.M73.V2500						2500	18.70
A100.M70.V1500					−7.0	1500	8.38
A100.M70.V2000						2000	10.15
A100.M70.V2500						2500	11.78
A100.M67.V1500					−6.7	1500	5.28
A100.M67.V2000						2000	6.40
A100.M67.V2500						2500	7.42
A125.M73.V1500	125	6.3	0.08	1.5	−7.3	1500	9.43
A125.M73.V2000						2000	11.43
A125.M73.V2500						2500	13.26
A125.M70.V1500					−7.0	1500	5.94
A125.M70.V2000						2000	7.20
A125.M70.V2500						2500	8.35
A125.M67.V1500					−6.7	1500	3.74
A125.M67.V2000						2000	4.54
A125.M67.V2500						2500	5.26

fractions, C III was included, but proved to be negligible and to have no important effect on the ionization fractions of C IV and C V. In models with $T_* = 100\,000$ K, C IV may become comparable to, or more important than C V, at some radial distance from the star. In the $T_* = 100\,000$ K models where this distance is not very large, we added C III in the calculations. As shown in Fig. 4, the ionization fraction of C III is only $\sim 10^{-4}$ in the outer parts of the wind and even lower in the inner wind layers. Its inclusion caused no notable changes in the ionization fraction of the C IV ion and was therefore considered not essential in this temperature regime.

4 SPECTRAL DIAGNOSTICS OF $\dot{M}$ AND T_*

The preferred method of determining stellar temperatures is through the ionization balance of He and CNO elements. The observation of spectral lines from different ionization stages of the same element avoids the need for assuming abundance ratios. Consistency is achieved by the use of several diagnostic elements. However, in the spectra of [WC] CSPNe, not many elements show lines from

different ionization stages. Therefore, the existence or absence of features in the spectra due to ions of different ionization potentials, along with the general appearance of the spectral lines, is also used as a temperature diagnostic.

In these stars, both photospheric and wind parameters affect the spectral features. Since several parameters can affect a spectral line, the identification of lines which are particularly sensitive to one parameter in a given regime is important for constraining its value. By examining the far-UV, UV and optical synthetic spectra produced for the grid, we identified spectral features sensitive to the mass-loss rate and stellar temperature and selected those most useful for placing constraints on their values. These are discussed in Sections 4.1 and 4.2.

4.1 [WCE] types

The far-UV, UV and optical spectra of [WCE] CSPNe are particularly poor in lines of multiple ionization stages of the same element. Only oxygen, neon and nitrogen show lines from multiple stages,

Table 2. Track B stellar parameters of the grid models for CSPNe with 0.6 M$_\odot$.

Model	T_* (kK)	$\log(g)$	R_* (R$_\odot$)	L_* (10^3 L$_\odot$)	$\log(\dot{M})$ (M$_\odot$ yr^{-1})	v_∞ (km s^{-1})	R_t (R$_\odot$)
B50.M70.V500	50	4.0	1.29	9.2	−7.0	500	43.80
B50.M70.V1000[a]						1000	69.53
B50.M63.V500					−6.3	500	14.98
B50.M63.V1000[a]						1000	23.78
B50.M60.V500					−6.0	500	9.45
B50.M60.V1000[a]						1000	14.99
B65.M70.V500	65	4.4	0.82	10.5	−7.0	500	27.86
B65.M70.V1000[a]						1000	44.23
B65.M63.V500					−6.3	500	9.53
B65.M63.V1000[a]						1000	15.13
B65.M60.V500					−6.0	500	6.01
B65.M60.V1000[a]						1000	9.53
B80.M70.V500	80	4.8	0.52	9.6	−7.0	500	17.59
B80.M70.V1000[a]						1000	27.92
B80.M63.V500					−6.3	500	6.02
B80.M63.V1000[a]						1000	9.55
B80.M60.V500					−6.0	500	3.79
B80.M60.V1000[a]						1000	6.02
B100.M70.V1500	100	5.3	0.29	7.4	−7.0	1500	20.54
B100.M70.V2000						2000	24.88
B100.M70.V2500[a]						2500	28.87
B100.M67.V1500					−6.7	1500	12.94
B100.M67.V2000						2000	15.67
B100.M67.V2500[a]						2500	18.19
B100.M65.V1500					−6.5	1500	9.87
B100.M65.V2000						2000	11.96
B100.M65.V2500[a]						2500	13.88
B125.M70.V1500	125	5.7	0.18	7.2	−7.0	1500	12.95
B125.M70.V2000						2000	15.68
B125.M70.V2500[a]						2500	18.20
B125.M67.V1500					−6.7	1500	8.16
B125.M67.V2000						2000	9.88
B125.M67.V2500[a]						2500	11.46
B125.M65.V1500					−6.5	1500	6.22
B125.M65.V2000						2000	7.54
B125.M65.V2500[a]						2500	8.75
B150.M70.V1500	150	6.0	0.12	7.0	−7.0	1500	8.85
B150.M70.V2000						2000	10.72
B150.M70.V2500[a]						2500	12.44
B150.M67.V1500					−6.7	1500	5.58
B150.M67.V2000						2000	6.76
B150.M67.V2500[a]						2500	7.84
B150.M65.V1500					−6.5	1500	4.26
B150.M65.V2000						2000	5.16
B150.M65.V2500[a]						2500	5.98
B165.M70.V1500	165	6.3	0.09	5.8	−7.0	1500	6.67
B165.M70.V2000						2000	8.08
B165.M70.V2500[a]						2500	9.37
B165.M70.V3000						3000	10.58
B165.M67.V1500					−6.7	1500	4.20
B165.M67.V2000						2000	5.09
B165.M67.V2500[a]						2500	5.90
B165.M67.V3000						3000	6.67
B165.M65.V1500					−6.5	1500	3.21
B165.M65.V2000						2000	3.88
B165.M65.V2500[a]						2500	4.51
B165.M65.V3000						3000	5.09

Table 2 – *continued*

Model	T_* (kK)	$\log(g)$	R_* (R$_\odot$)	L_* (10^3 L$_\odot$)	$\log(\dot{M})$ (M$_\odot$ yr^{-1})	v_∞ (km s^{-1})	R_t (R$_\odot$)
B200.M73.V1500	200	7.0	0.04	2.4	−7.3	1500	4.60
B200.M73.V2000						2000	5.57
B200.M73.V2500						2500	6.47
B200.M73.V3000						3000	7.31
B200.M70.V1500					−7.0	1500	2.90
B200.M70.V2000						2000	3.51
B200.M70.V2500[a]						2500	4.08
B200.M70.V3000						3000	4.60
B200.M67.V1500					−6.7	1500	1.83
B200.M67.V2000						2000	2.21
B200.M67.V2500[a]						2500	2.57
B200.M67.V3000						3000	2.90
B200.M65.V1500					−6.5	1500	1.39
B200.M65.V2000						2000	1.69
B200.M65.V2500[a]						2500	1.96
B200.M65.V3000						3000	2.21

[a]Models with different neon abundances are also available.

Table 3. Track C stellar parameters of the grid models for CSPNe with 0.9 M$_\odot$.

Model	T_* (kK)	$\log(g)$	R_* (R$_\odot$)	L_* (10^3 L$_\odot$)	$\log(\dot{M})$ (M$_\odot$ yr^{-1})	v_∞ (km s^{-1})	R_t (R$_\odot$)
C100.M67.V1500	100	4.8	0.62	33.5	−6.7	1500	27.59
C100.M67.V2000						2000	33.42
C100.M67.V2500						2500	38.79
C100.M65.V1500					−6.5	1500	21.06
C100.M65.V2000						2000	25.51
C100.M65.V2500						2500	29.60
C100.M64.V1500					−6.4	1500	17.38
C100.M64.V2000						2000	21.06
C100.M64.V2500						2500	24.44
C125.M67.V1500	125	5.3	0.35	25.8	−6.7	1500	15.47
C125.M67.V2000						2000	18.75
C125.M67.V2500						2500	21.75
C125.M65.V1500					−6.5	1500	11.81
C125.M65.V2000						2000	14.31
C125.M65.V2500						2500	16.60
C125.M64.V1500					−6.4	1500	9.75
C125.M64.V2000						2000	11.81
C125.M64.V2500						2500	13.70
C165.M67.V1500	165	5.7	0.22	31.2	−6.7	1500	9.75
C165.M67.V2000						2000	11.82
C165.M67.V2500						2500	13.71
C165.M67.V3000						3000	15.48
C165.M65.V1500					−6.5	1500	7.44
C165.M65.V2000						2000	9.03
C165.M65.V2500						2500	10.46
C165.M65.V3000						3000	11.82
C165.M64.V1500					−6.4	1500	6.14
C165.M64.V2000						2000	7.44
C165.M64.V2500						2500	8.64
C165.M64.V3000						3000	9.75
C200.M67.V1500	200	6.0	0.15	33.8	−6.7	1500	6.90
C200.M67.V2000						2000	8.36
C200.M67.V2500						2500	9.71
C200.M67.V3000						3000	10.96

Table 3 – *continued*

Model	T_* (kK)	$\log(g)$	R_* (R$_\odot$)	L_* (10^3 L$_\odot$)	$\log(\dot{M})$ (M$_\odot$ yr^{-1})	v_∞ (km s^{-1})	$R_{\rm t}$ (R$_\odot$)
C200.M65.V1500					−6.5	1500	5.27
C200.M65.V2000						2000	6.38
C200.M65.V2500						2500	7.41
C200.M65.V3000						3000	8.36
C200.M64.V1500					−6.4	1500	4.35
C200.M64.V2000						2000	5.27
C200.M64.V2500						2500	6.11
C200.M64.V3000						3000	6.90
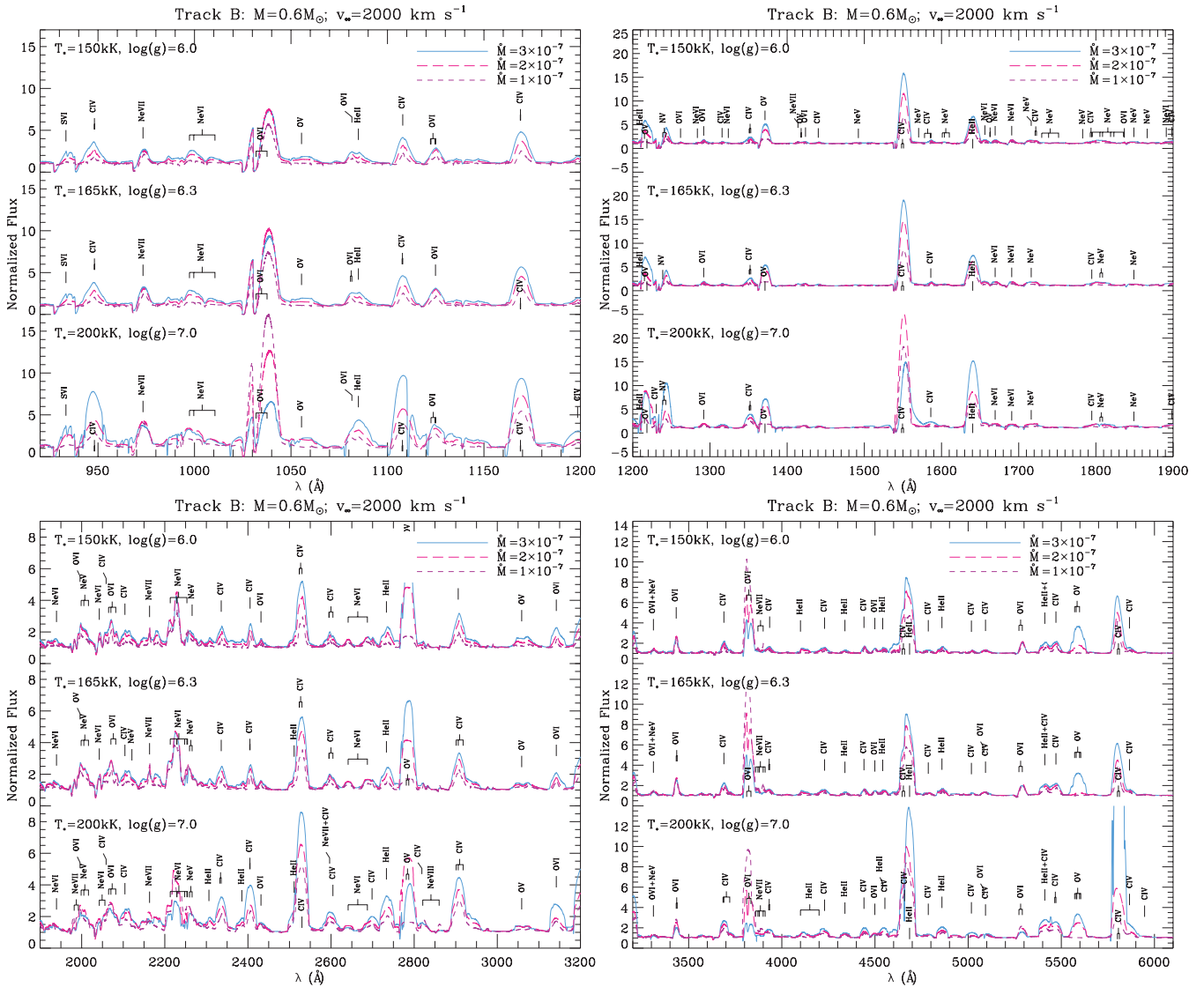
Figure 2. Examples of plots comparing different grid models, from the far-UV to the optical range. Here and in subsequent figures, mass-loss rates are given in M$_\odot$ yr^{-1}. Similar plots for all grid models are available online.

yet only oxygen presents strong lines throughout the whole temperature range considered.

Several other lines can be used as diagnostics of photospheric and wind parameters. The He II lines λ1640.4 and λ4685.7 Å (the last one appears blended with a strong C IV line at λ4658.9 Å, since in [WCE] stars, the wind's terminal velocities are high) are mostly sensitive to mass-loss and show little sensitivity to the temperature in the regime between $T_* = 100\,000$ and $165\,000$ K. This happens because, for these high temperatures, helium is almost totally ionized. Examples of line profiles are shown in Fig. 5, along with the helium ionization fractions, in which we see that the fraction of He II remains virtually unaltered in the hotter models.
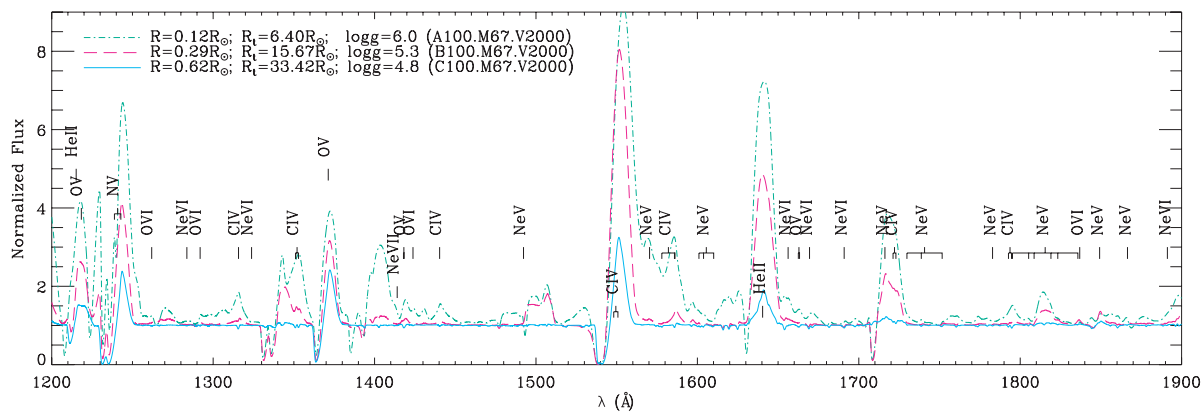
Figure 3. Models A100.M67.V2000, B100.M67.V2000 and C100.M67.V2000, with $T = 100$ kK, $\dot{M} = 2 \times 10^{-7}$ M$_\odot$ yr^{-1} and $v_\infty = 2000$ km s^{-1}, differing in R, R_t and log g. Wind features vary greatly due to the different wind densities.

Table 4. Species considered in the calculation of the grid models.

Element	Ions
He	I, II, III
C	II^a, III^a, IV, V
N	II^a, III^a, IV^a, V, VI
O	II^a, III^a, IV^a, V, VI, VII
Ne	II^a, III^a, IV^a, V, VI, VII, VIII, IX
Al	III^a, IV^a, V^a
Si	III^a, IV, V^a, VI^a
P	IV^a, V, VI
S	III^a, IV^a, V^a, VI, VII
Fe	IV^a, V^a, VI^a, VII, VIII, IX, X, XI

^{a}These ionic species are not included in the calculation of all models. They were introduced where needed based on the analysis of the ionization fractions.
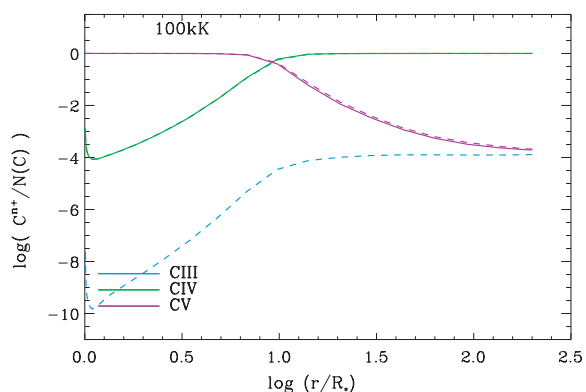
Figure 4. The C ionization fractions of two $T_* = 100\,000$ K models, with identical stellar parameters, and the C III ion included (dashed lines) or not included (solid lines) in the calculations.

Among all the spectral lines in the studied range, Ne VII λ973.3 Å shows the least sensitivity to mass-loss, which makes it a good indicator of temperature within the range of physical parameters studied here. Its behaviour is shown in the top left-hand panel of

Fig. 6. Herald et al. (2005) and Bianchi & Herald (2007) found, however, that it can be sensitive to the neon abundance in PG1159 spectra, when it is not saturated. In Section 4.3, we discuss the effect of the neon abundance in the grid models.

For the O VI $\lambda\lambda$1031.9, 1037.6 Å doublet shown in Fig. 7 (top left-hand panel), both the temperature and mass-loss alter the line profiles significantly. The O VI $\lambda\lambda$3811.4, 3834.2 Å lines, seen in Fig. 7 (bottom right-hand panel), show little variability with mass-loss, within the range of values analysed, in the two cooler models. In the hotter models, on the other hand, it shows a behaviour opposite to that of all other strong lines in the range studied here, the line intensity decreasing with increasing mass-loss. Also, the large variation in the line profile between models with temperatures of 125 000 and 150 000 K can help establish lower or higher limits for the temperature. In the bottom panels of Fig. 7, we show oxygen ionization fraction plots for different temperatures and mass-loss rates. We see that the O VI ion gains importance as we progress towards higher temperatures, which is reflected in the increasing intensity of the O VI lines in the hotter models. The mass-loss rate, on the other hand, has a more complex effect on these lines: it alters not only the density of the ion in the expanding atmosphere, but also its temperature structure, altering the ionization fractions. Denser winds will be cooler, with lower ionic species growing in importance. For massive stars, the O VI $\lambda\lambda$1031.9, 1037.6 Å lines were found to strongly depend on X-rays and to have a hard threshold with mass-loss, while other lines strongly depend on clumping (Bianchi & Garcia 2002). The effect of X-rays on the far-UV O VI doublet will be discussed in Section 4.4.

Other temperature indicators are the neon and oxygen features shown in Figs 6 (top right-hand panel) and 7 (middle left-hand panels), respectively. These features are due to O IV (with lines at $\lambda\lambda$3403.6, 3411.7, 3413.6 Å), O VI (at λ3433.3 Å) and Ne VI (with contamination by Ne V lines). The Ne VI feature can only be seen in hotter models ($T_* \geq 150\,000$ K). The O IV feature appears only in the two cooler ones (for $T_* = 100\,000$ and 125 000 K), while it is substituted by the O VI line as the temperature increases. For the right combination of mass-loss and temperature, these oxygen lines can also coexist. Thus, these features can be used to constrain the temperature regime of the object being studied. Also seen in the middle left-hand panels of Fig. 7 are the Ne V λ3313.7 Å and N IV $\lambda\lambda$3478.7, 3483.0, 3484.9 Å lines, which can help constrain neon and nitrogen abundances.

The strong C IV doublet at $\lambda\lambda$1548.2, 1550.8 Å shows sensitivity to both mass-loss and temperature, as can be seen in the
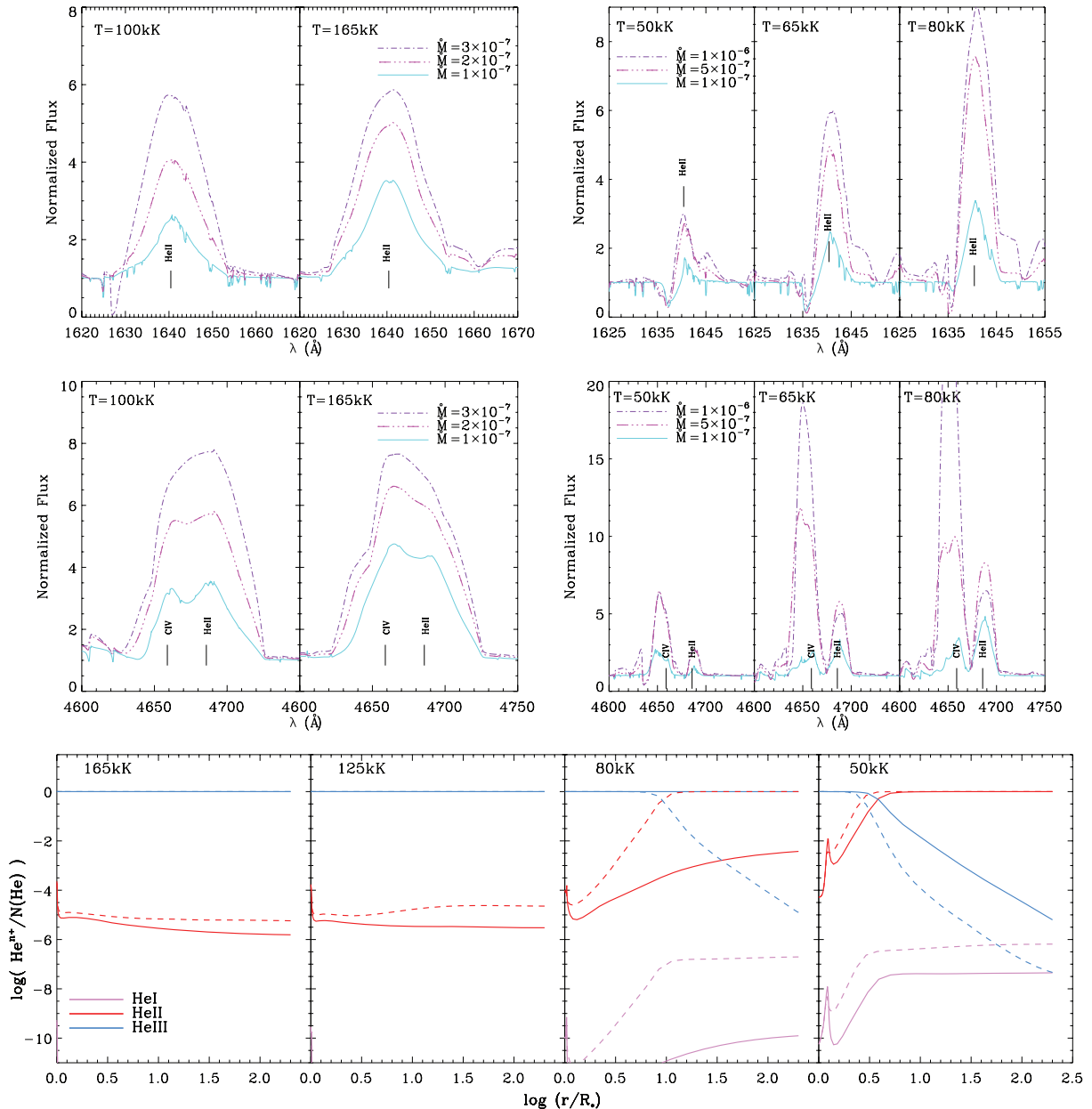
Figure 5. Model profiles of the He II lines λ1640.4 Å (top panels) and λ4685.7 Å (middle panels) at different temperatures (also radii) and mass-loss rates. The bottom panels display the ionization fractions of helium, where the continuous lines indicate models with $\dot{M} = 10^{-7}$ M$_\odot$ yr^{-1} and the dashed lines indicate $\dot{M} = 10^{-6}$ M$_\odot$ yr^{-1} for models with $T_* \leq 80$ kK or $\dot{M} = 3 \times 10^{-7}$ M$_\odot$ yr^{-1} for models with $T_* \geq 100$ kK. All the models shown belong to track B ($M_* = 0.6$ M$_\odot$) and have $v_\infty = 2500$ km s^{-1}.

middle left-hand panel of Fig. 8. Nevertheless, once either mass-loss or temperature is established through other indicators, it can help constrain the other parameter. Also, this line is an important diagnostic of the wind's terminal velocity, since this ion is abundant also in the outer parts of the wind down to temperatures of 50 000 K.

4.2 [WCL] types

The winds of [WCL] CSPNe are characterized by much lower terminal velocities than the ones of [WCE] stars, which results in narrower spectral lines. Also, these cooler CSPNe seem to show a wider range in mass-loss, by comparing results of spectral analyses

found in the literature. We took these facts into consideration when calculating the grid.

These objects present very complex spectra and a higher number of spectral lines from elements with multiple ionization stages, thus making the stellar temperature easier to constrain. Several strong C III and C IV lines appear in the grid models for these stars, along with multiple ionization stages of neon, nitrogen, oxygen, phosphorus, sulphur and helium.

We selected some spectral features useful for distinguishing temperatures and mass-loss rate values, within the regime considered. The top left-hand panel of Fig. 8 shows a section of the optical spectra where strong lines from both C III (λ5695.9 Å) and C IV (λλ5801.3, 5812.0, 5865.9 Å) can be seen, along with
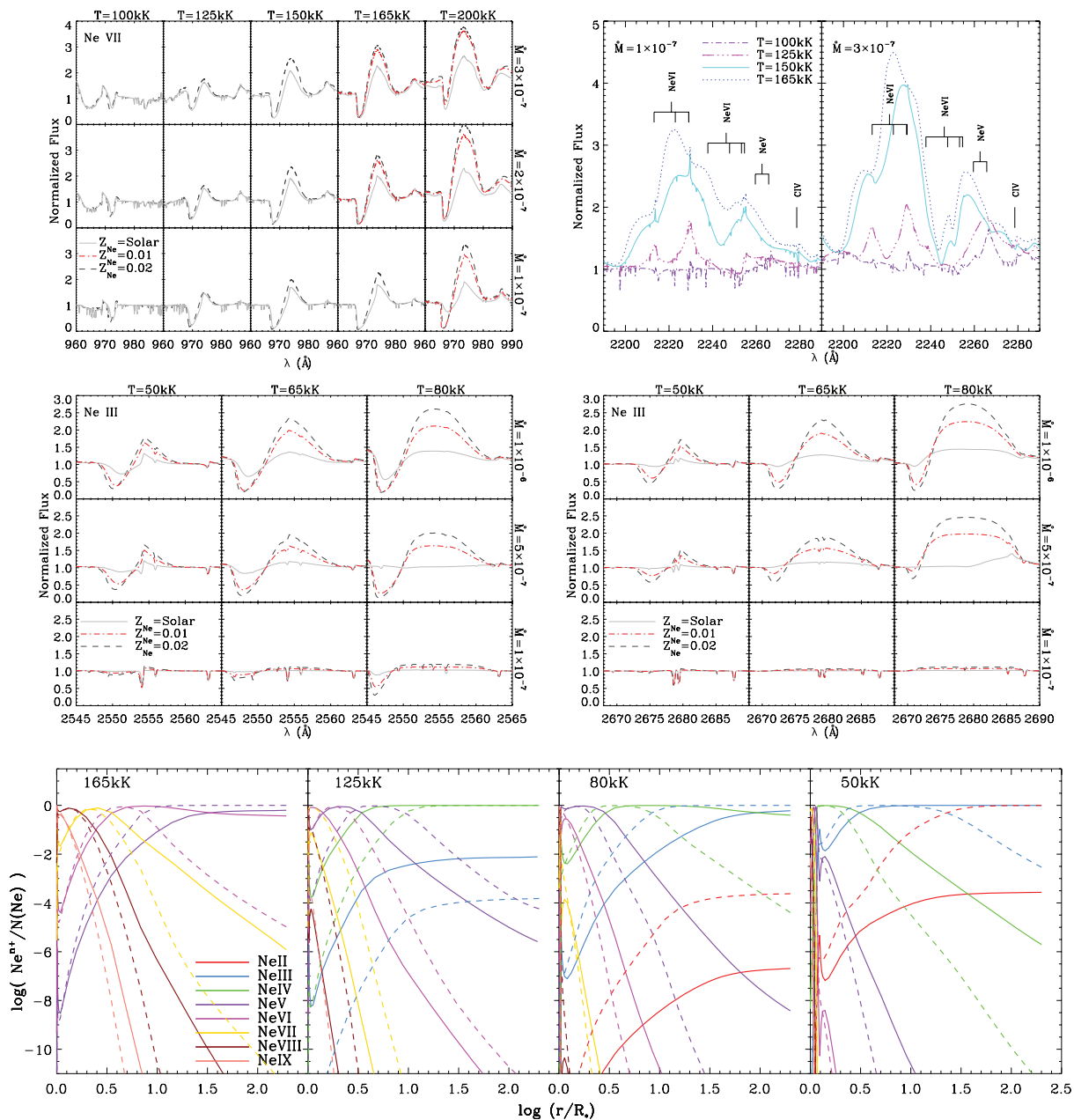
Figure 6. Ne lines from different ionization stages and their variation with temperature (also radius), mass-loss rate and neon abundance. In the top left-hand panel, for clarity, the models with $X_{Ne} = 0.01$ were omitted when the effect of Ne abundance is small. The bottom panels show the ionization fractions of neon (for models with a neon mass fraction of $X_{Ne} = 0.02$): the continuous lines indicate models with $\dot{M} = 10^{-7}\,M_\odot\,yr^{-1}$ and the dashed lines indicate $\dot{M} = 10^{-6}\,M_\odot\,yr^{-1}$ for models with $T_* \leq 80\,kK$ or $\dot{M} = 3 \times 10^{-7}\,M_\odot\,yr^{-1}$ for models with $T_* \geq 100\,kK$. All the models shown are from track B ($M_* = 0.6\,M_\odot$) and have $v_\infty = 2500\,km\,s^{-1}$.

a He I line ($\lambda 5875.7\,\text{Å}$), making this spectral region an important diagnostic of the stellar temperature. The O IV $\lambda\lambda 3403.6$, 3411.7, 3413.6 Å spectral features shown in the middle right-hand panel of Fig. 7 are likewise an excellent indicator of the stellar temperature between $T_* = 50\,000$ and $80\,000\,K$, showing very little sensitivity to the mass-loss rate in the interval studied. Also shown is the N IV $\lambda 3478.7\,\text{Å}$ line.

In the late [WC] type, the O VI $\lambda\lambda 1031.9$, 1037.6 Å doublet, shown in Fig. 7 (top right-hand panel) is still present, albeit much weaker and showing contamination by other spectral lines. Another useful diagnostic line for the [WCL] subclass is the C III $\lambda 1908.7\,\text{Å}$ line shown in the top right-hand panel of Fig. 8. It is much more sensitive

to mass-loss than to temperature in the range shown, thus making it an important mass-loss discriminator.

Other lines such as He II $\lambda 1640.4\,\text{Å}$ (shown in the top right-hand panel of Fig. 5), He II $\lambda 4685.7\,\text{Å}$ and C IV $\lambda 4658.9\,\text{Å}$ (middle right-hand panel of Fig. 5), O III $\lambda\lambda 1150.9$, 1153.8 Å (bottom left-hand panel of Fig. 7, also showing a Ne V line at $\lambda 1146.1\,\text{Å}$), C IV $\sim \lambda 1169\,\text{Å}$ and C III $\sim \lambda 1176\,\text{Å}$ (both of them are blends of several lines), and C III $\lambda 2296.9\,\text{Å}$ (Fig. 8, middle right-hand and bottom panels) show high sensitivity to both mass-loss and temperature. Nevertheless, once the temperature or mass-loss is constrained by other indicators, they can be an important diagnostic of the remaining parameter.
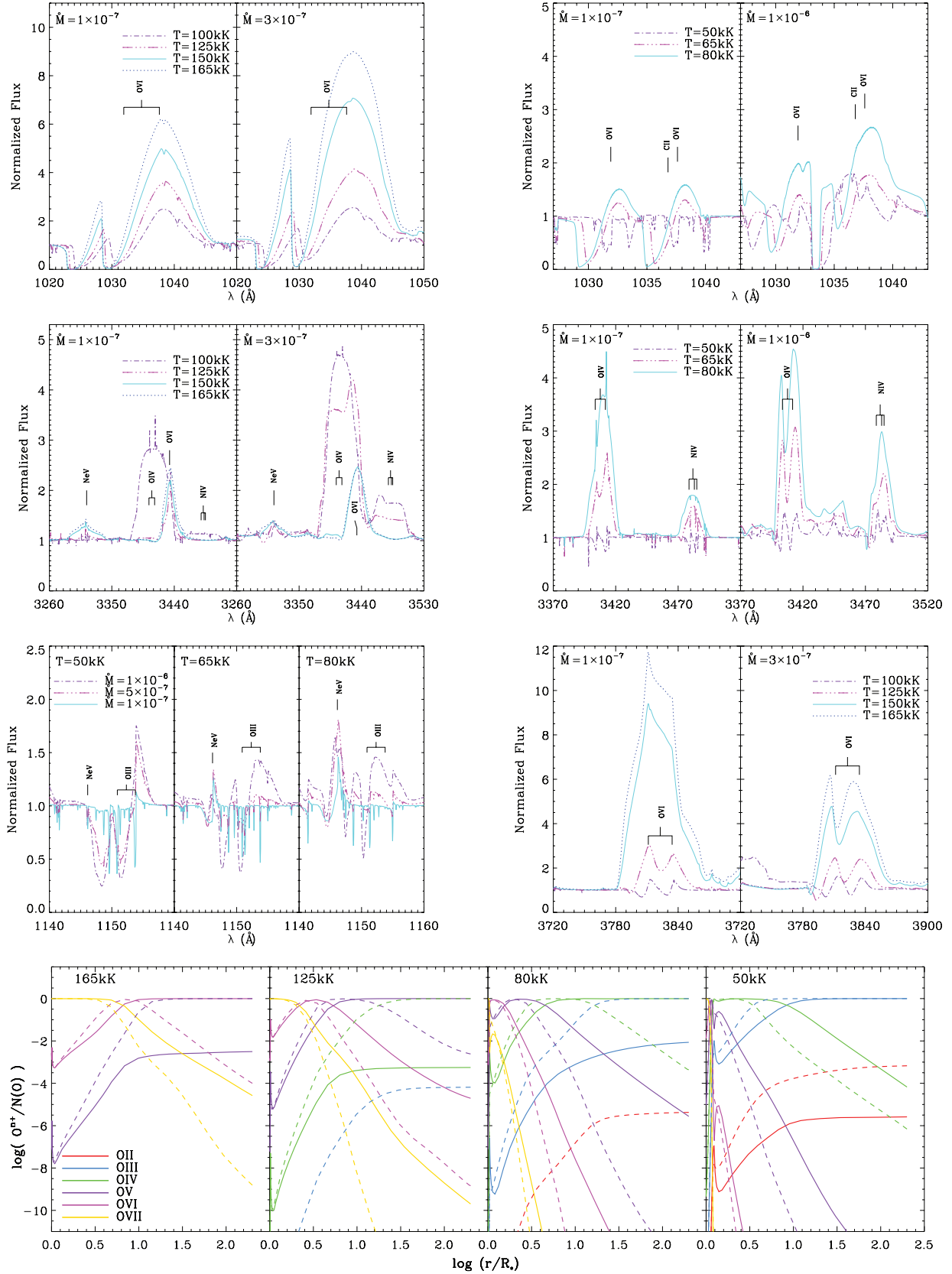
Figure 7. Synthetic line profiles from different ionization stages of oxygen in various models. The bottom panels show the ionization fractions of oxygen: the continuous lines indicate models with $\dot{M} = 10^{-7}$ M$_\odot$ yr^{-1} and the dashed lines indicate $\dot{M} = 10^{-6}$ M$_\odot$ yr^{-1} for models with $T_* \leq 80$ kK or $\dot{M} = 3 \times 10^{-7}$ M$_\odot$ yr^{-1} for models with $T_* \geq 100$ kK. All the models shown are from track B ($M_* = 0.6$ M$_\odot$) and have $v_\infty = 2500$ km s^{-1}.
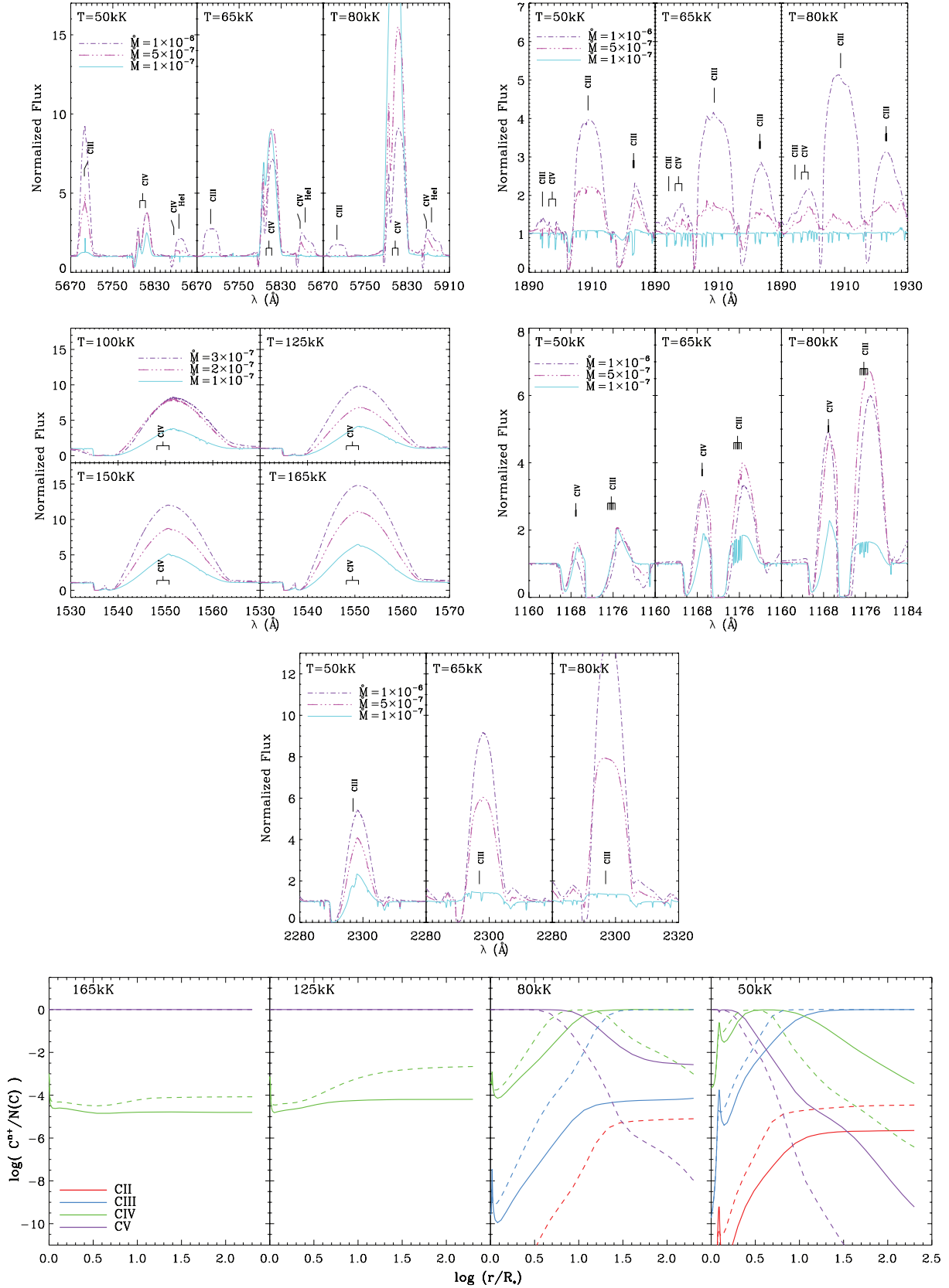
Figure 8. Profiles of carbon lines of different ionization stages from models with different mass-loss rates and temperatures (also radii). The bottom panels show the ionization fractions of carbon: the continuous lines indicate models with $\dot{M} = 10^{-7}$ M$_\odot$ yr^{-1} and the dashed lines indicate $\dot{M} = 10^{-6}$ M$_\odot$ yr^{-1} for models with $T_* \leq 80$ kK or $\dot{M} = 3 \times 10^{-7}$ M$_\odot$ yr^{-1} for models with $T_* \geq 100$ kK. All the models shown are from track B ($M_* = 0.6$ M$_\odot$) and have $v_\infty = 2500$ km s^{-1}.
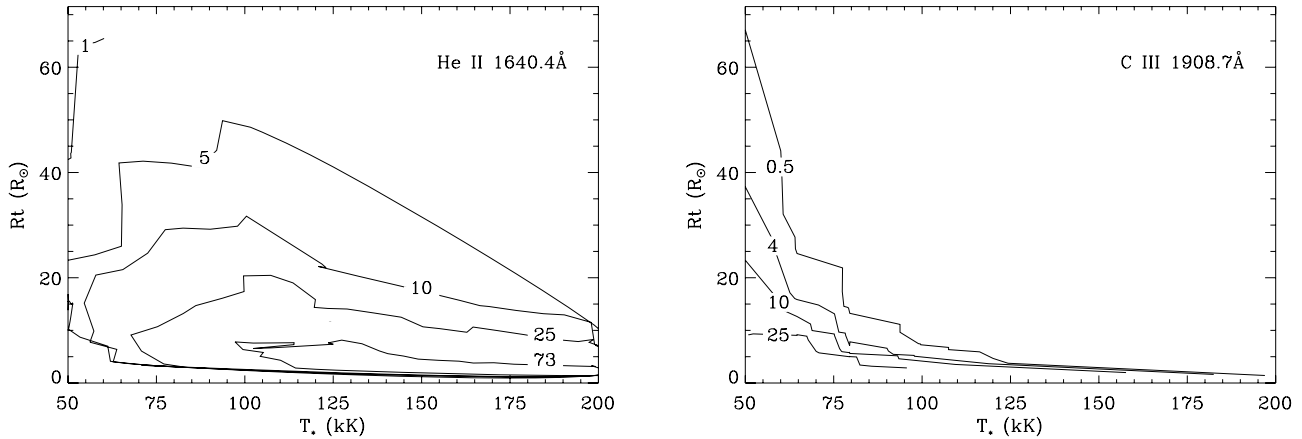
Figure 9. Contours of constant equivalent widths for He II λ1640.4 Å and C III λ1908.7 Å emission lines. Labels are in Å.

In order to further visualize the dependence of spectral diagnostics on the photospheric and wind parameters, we made contour plots of the equivalent widths of two spectral lines discussed in this section, having the stellar temperature and transformed radius on the axes. Contour plots of the He II λ1640.4 Å line and the C III λ1908.7 Å line are shown in Fig. 9, where the contours indicate the equivalent widths of the lines. In the case of P Cygni profiles, CMFGEN calculates the equivalent widths of a line by subtracting that of the absorption component from that of the emission. These two lines are very sensitive to mass-loss in the [WCE] and [WCL] parameter regimes, respectively, and thus can be used to identify the interval of the transformed radius and temperature that matches the data.

4.3 Effect of Ne abundance

A Ne abundance of the order of 2 per cent by mass is expected from evolutionary models for the [WC] stars, which present in their surfaces the abundance pattern of the region between the hydrogen- and helium-burning shells of the precursor AGB star. In AGB stars, neon is produced from nitrogen through the $^{14}N(\alpha, \gamma)^{18}F(\beta^+)^{18}O(\alpha, \gamma)^{22}Ne$ chain in the helium-burning shell and then dredged up to the convective intershell (see e.g. Werner & Herwig 2006). Thus, the determination of neon abundances is important to constrain evolutionary models, in particular, the dredge-up episodes. Also, the presence of several ionization stages of neon in the winds of [WCE] stars is potentially a useful tool for the determination of the stellar temperature. In Fig. 6, we show several neon features present in the models in different temperature and mass-loss regimes, for different values of neon abundance, ranging from solar to 11.5 times supersolar (which is adopted for the models in the grid). In the top left-hand panel, the Ne VII λ973.3 Å line seen in the grid models for [WCE] stars shows little sensitivity to neon abundance in the models with $T_* = 100\,000$ and 125 000 K. For higher temperatures, this line starts to show a higher sensitivity to Ne abundances and can potentially help constrain it. Also, if used together with neon lines from different ionization stages, it can contribute to the determination of the stellar temperature, although it also depends on the mass-loss rate.

In the middle right-hand and left-hand panels of Fig. 6, we show the Ne III lines, which appear in the synthetic spectra for the [WCL] subclass at λ2553.4 Å and at λλ2677.9, 2678.6 Å, respectively. Both lines present high sensitivity to the neon abundance, temperature and mass-loss rate, and are therefore useful to constrain the neon

abundance when the photospheric and wind parameters have been determined through other indicators. They also help in the determination of the stellar temperature when used in conjunction with other neon lines of different ionization stages.

4.4 Effect of X-rays

X-ray emission of the order of $L_X \sim 10^{-7} L_*$ observed in massive O- and B-type stars (Chlebowski, Harnden & Sciortino 1989; Chlebowski & Garmany 1991; Evans et al. 2003) is commonly believed to originate from shocks in the stellar wind, which form due to the unstable nature of the radiative force on spectral lines (Lucy & White 1980; Owocki et al. 1988). Such a flux of X-ray photons has been invoked in order to reproduce the strong O VI λλ1031.9, 1037.6 Å doublet in early-O-type stars and to achieve consistency among observed N V, Si IV and C IV diagnostics (Garcia & Bianchi 2004; Bianchi et al. 2009).

Since the fast winds of CSPNe are also believed to be subjected to the radiation pressure in spectral lines, they are expected to be clumped and may exhibit X-ray fluxes. Guerrero et al. (2001) measured an X-ray luminosity of $\sim 10^{-7} L_*$ for the central star of NGC 6543, consistent with that predicted from shocks in the stellar wind. However, the emission could also be explained by the coronal activity of an undetected companion.

We examined the effect of soft X-ray fluxes in the synthetic spectra computed for our grid. We recomputed models with $T_* = 65\,000$, 100 000 and 165 000 K including soft X-ray fluxes into the calculations. We assumed the shock temperatures of 5×10^6 and 3×10^6 K, starting at the velocities of 300 and 400 km s^{-1}, respectively. In the model with $T_* = 165\,000$ K, only an extremely-high X-ray flux yielding an observed X-ray luminosity of $\sim 10^{-2} L_*$ (for a mass-loss rate of 1.0×10^{-7} M$_\odot$ yr^{-1}), caused a relevant effect on the spectra, mainly in the O VI λλ1031.9, 1037.6 Å doublet, as shown in Fig. 10. In models with progressively lower temperatures, we found that lower X-ray luminosities modify the O VI doublet profile. For the $T_* = 100\,000$ K model, a reasonable X-ray luminosity of $\sim 10^{-7} L_*$ (for $\dot{M} = 1.0 \times 10^{-7}$, 2.0×10^{-7} and 3.0×10^{-7} M$_\odot$ yr^{-1}) significantly alters the O VI doublet (but not other spectral features), as shown in Fig. 10. At a temperature of $T_* = 65\,000$ K, the convergence of models with X-ray fluxes proved to be very hard to reach. Nevertheless, we were able to obtain a converged model for a mass-loss rate of $\dot{M} = 5.0 \times 10^{-8}$ M$_\odot$ yr^{-1} with an X-ray luminosity of $4 \times 10^{-10} L_*$. Again, the only spectral
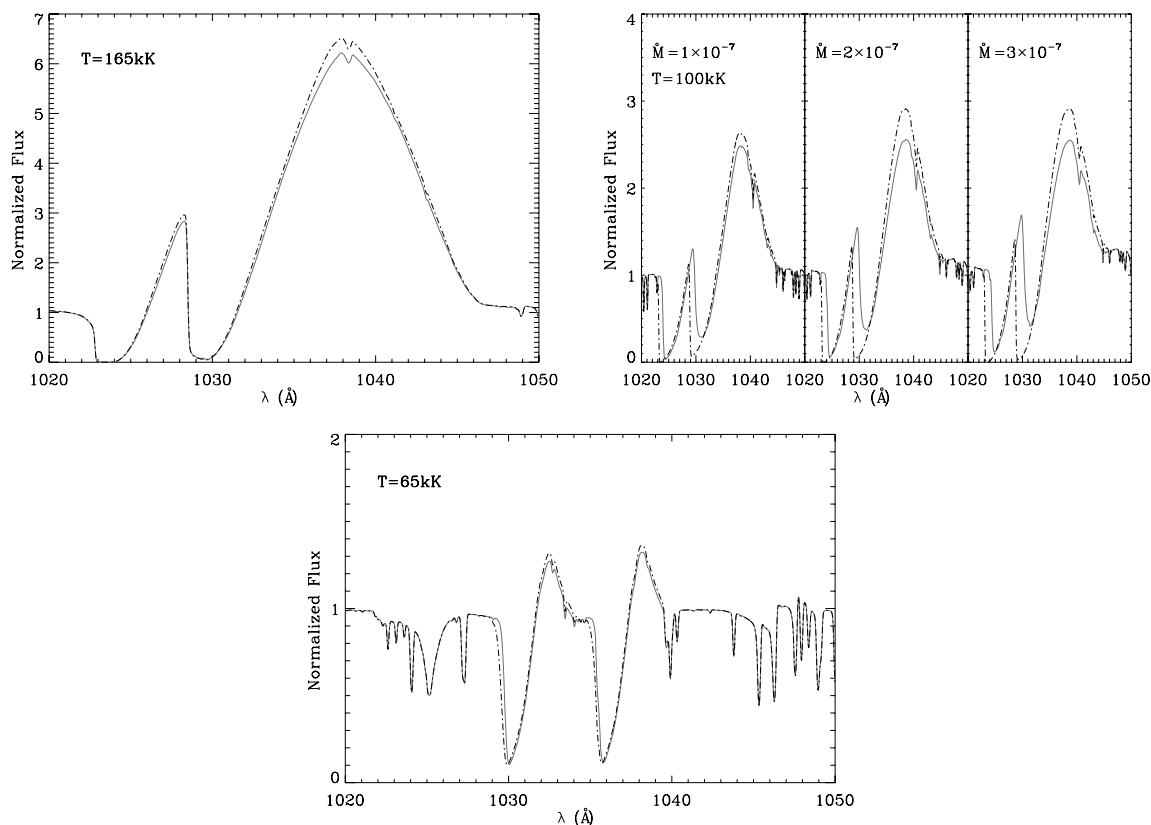
Figure 10. Comparison between models with (dot–dashed line) and without (continuous line) X-rays. The O VI λλ1031.9, 1037.6 Å doublet is shown due to its sensitivity to X-ray ionization (see text). For the $T_* = 165$ kK model, an extreme X-ray luminosity of $\sim 10^{-2}L_*$ is shown, for the $T_* = 100$ kK models, we show $L_X \sim 10^{-7}L_*$ and for the $T_* = 65$ kK model, $L_X = 4 \times 10^{-10}L_*$.

feature affected was the far-UV O VI doublet, which is also shown in Fig. 10.

5 SPECTRAL ANALYSIS OF THE CENTRAL STAR OF NGC 6905

To illustrate the usefulness of the model grid, we apply it here to derive the physical parameters of the [WCE] central star of NGC 6905. We compare our grid models with data (Table 5) available at the Multimission Archive at the Space Telescope Science Institute (STScI) (MAST) from *FUSE* and *HST* spectrographs. The *FUSE* covers the wavelength range 905–1187 Å with a resolving power of $\lesssim 20\,000$. We also used *HST*-STIS spectra obtained with the *G140L* ($R \sim 1200$) and *G230L* ($R \sim 750$) gratings with a wavelength coverage of 1150–1736 and 1570–3180 Å, respectively. In all figures showing the observed spectra of NGC 6905, the resolution of the models, in the STIS wavelength range, is matched to the resolution of the observations by convolving the synthetic spectra with the instrument line spread functions, while for the spectral region covered by the *FUSE*, which is full of interstellar hydrogen absorp-

tions, the models and observations were convolved with a Gaussian of full width at half-maximum =0.1 Å to facilitate the visualization. In Figs 11–20, the interstellar absorption was omitted from the synthetic spectra to facilitate the visualization and will be further discussed below. The line identifications in these figures only mark the strongest lines in each model.

We obtained an initial estimate of the wind's terminal velocity by measuring the blue edge velocity, v_{edge}, from the strong P Cygni profile of the C IV λ1548.2 Å line. We derived $v_\infty = 2170$ km s^{-1}, correcting v_{edge} for an assumed turbulence velocity, v_{turb}, of 10 per cent v_∞ (Lamers & Cassinelli 1999):

$$v_\infty \simeq v_{\text{edge}} - 2 \times v_{\text{turb}}. \tag{6}$$

This estimate is confirmed by comparing the observed spectra with grid models computed for wind's terminal velocities $v_\infty = 2500$, 2000 and 1500 km s^{-1}. An example is shown in Fig. 11.

We then used the grid of models with the appropriate wind's terminal velocity to constrain the temperature and the transformed radius of the central star of NGC 6905. Based on these results, we

Table 5. Spectra of NGC 6905's central star used in the analysis.

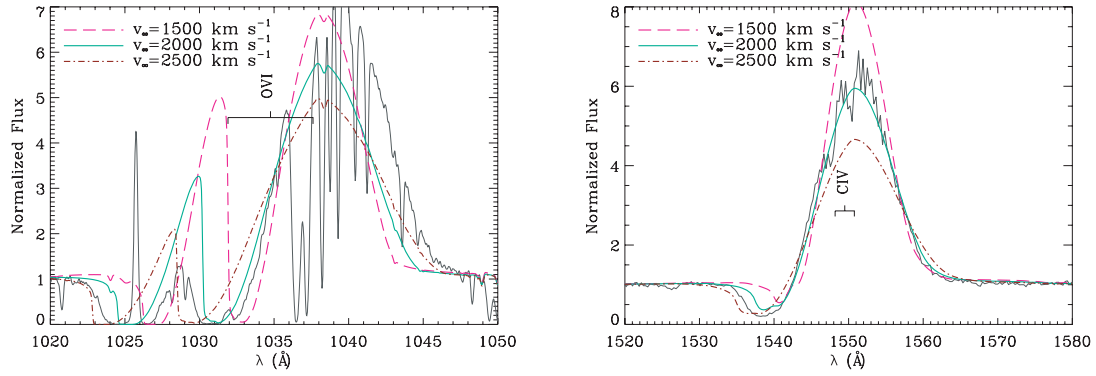| Instrument	Data set	Date	Resolution (Å)	Aperture (arcsec)	Range (Å)
FUSE	A1490202000	2000 August 11	∼0.06	30×30	905–1187
STIS + G140L	O52R01020	1999 June 29	∼1.20	52×0.5	1150–1736
STIS + G230L	O52R01010	1999 June 29	∼3.15	52×0.5	1570–3180

Figure 11. The two lines showing the strongest observed (continuous black line) P Cygni profiles in the spectra of NGC 6905, O VI λλ1031.9, 1037.6 Å in the *FUSE* range and C IV λλ1548.2, 1550.8 Å in the STIS G140L range, are shown, as well as models computed with three values of v_∞ from our model grid. All other parameters in the models are identical and correspond to our derived values.
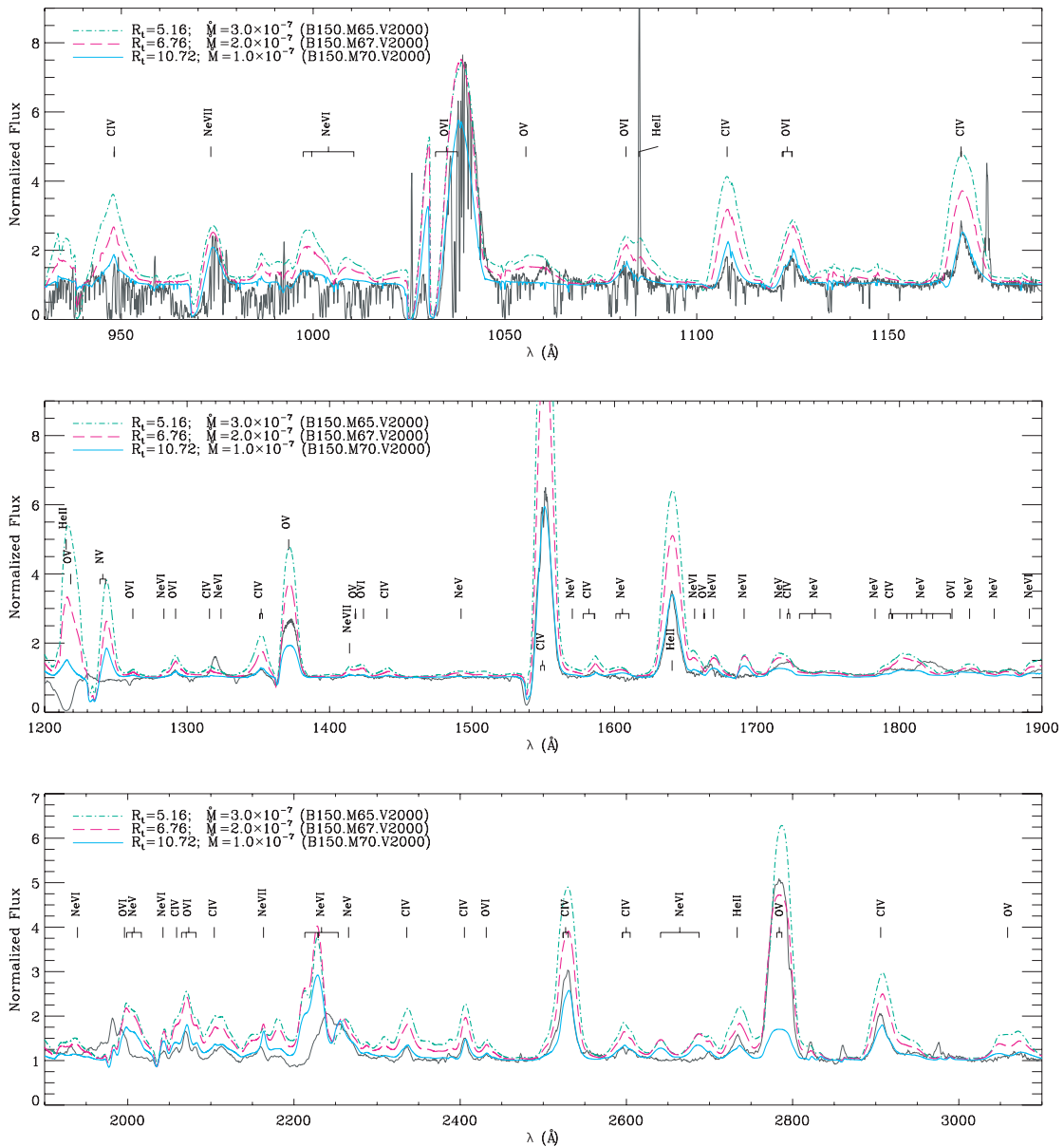

Figure 12. UV and far-UV observed spectra (continuous black line) of the central star of NGC 6905 and three models with $T_* = 150$ kK and different values of the transformed radius (transformed radius and mass-loss rate are given in units of $R_\odot$ and $M_\odot$ yr^{-1}, respectively). Among the grid models, the light blue continuous line is the one that fits best the observed diagnostics, except for the two O V lines which are better fitted by higher mass-loss rates and some weak neon features (discussed in the text).
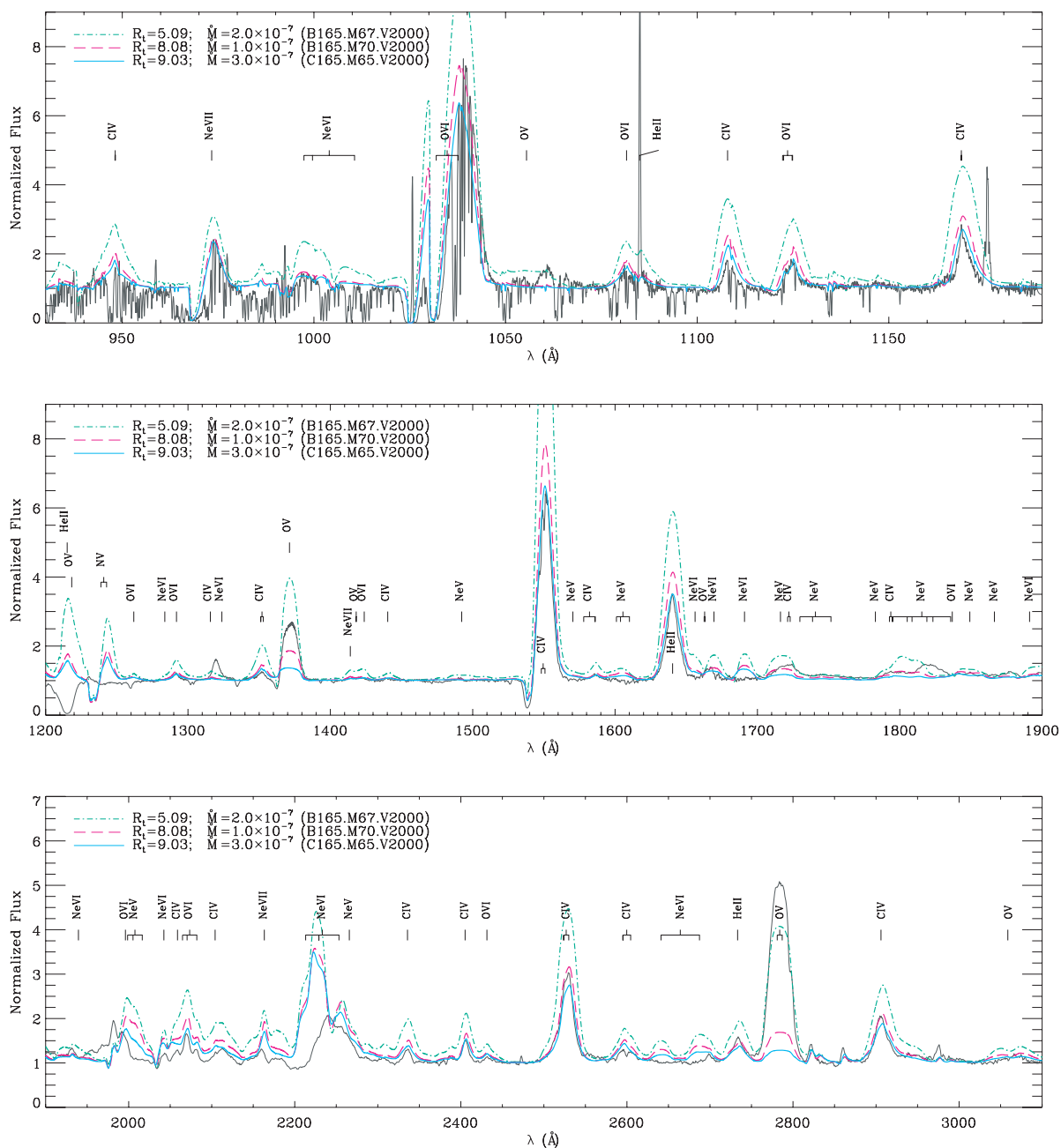
Figure 13. The UV and far-UV observed spectra of the CSPN NGC 6905 (continuous black line, as in Fig. 12) are shown along with three grid models with $T_* = 165$ kK and different values of the transformed radius. The discrepancy between the O v lines and all other diagnostics is even larger than for $T_* = 150$ kK models (Fig. 12).

then perform a more detailed analysis, varying additional parameters not explored by the grid.

5.1 Using the grid to constrain the temperature and transformed radius

The central star of NGC 6905 is a [WCE]; therefore, its spectra are poor in lines of multiple ions of the same element. Among the features identified in the spectra, only oxygen shows strong lines of multiple ionization stages. Several O vi lines are present ($\lambda\lambda1031.9, 1037.6$ Å; $\lambda\lambda1080.8, 1081.6$ Å; $\lambda\lambda1122.5, 1124.8, 1124.9$ Å; $\lambda1291.9$ Å; $\lambda1996.1$ Å; $\lambda2070.4$ Å; $\lambda2082.04$ Å;

$\lambda2431.409$ Å), along with two strong O v lines at $\lambda1371.3$ Å and $\lambda\lambda2781.0, 2787.0$ Å. However, as will be discussed below, these two O v lines are only matched by grid models incompatible with other spectral diagnostics and both show sensitivity to the inclusion of heavy elements in the calculations, while other lines do not. Therefore, they are more useful as an indirect indicator of abundance and not to uniquely constrain the temperature. Several C iv lines are also observed and used as temperature diagnostics.

As a first step, we compare the observed spectra of the central star of NGC 6905 with our grid models with a wind's terminal velocity of 2000 km s^{-1}, the closest value available in the grid to the one inferred from the C iv $\lambda1548.2$ Å P Cygni absorption edge.
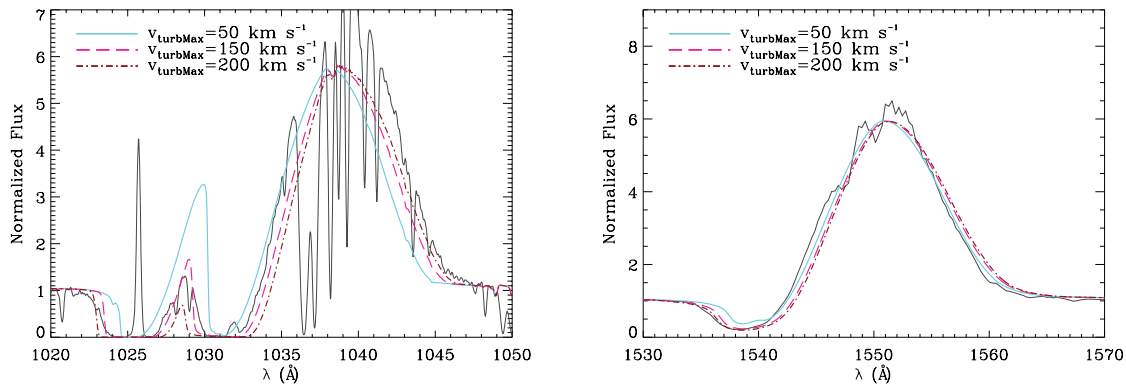
Figure 14. The two strongest P Cygni line profiles present in the observed spectra of NGC 6905 (continuous black line), O VI $\lambda\lambda1031.9$, 1037.6 Å and C IV $\lambda\lambda1548.2$, 1550.8 Å, are compared with models with $T_* = 150$ kK, $\dot{M} = 10^{-7}$ M$_\odot$ yr^{-1}, $v_\infty = 2000$ km s^{-1} and different turbulence velocities.

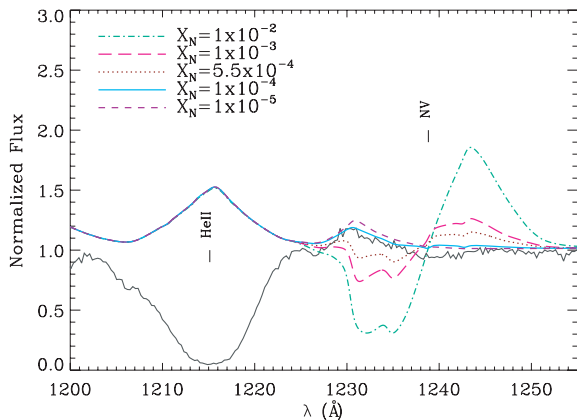**Figure 15.** The observed (continuous black line) Lyα interstellar absorption and the N V $\lambda\lambda1238.8$, 1242.8 Å doublet compared with models with $T_* = 150$ kK, $\dot{M} = 10^{-7}$ M$_\odot$ yr^{-1}, $v_\infty = 2000$ km s^{-1} and different values of nitrogen abundance.

The comparison rules out models with $T_* = 125\,000$ K, which show very weak O VI $\lambda\lambda1031.9$, 1037.6 Å lines, of about half the observed intensity, for all the mass-loss rate values in our grid, besides a too weak Ne VII $\lambda973.3$ Å line, which, as shown in Fig. 6, at this temperature, shows little sensitivity to mass-loss and neon abundance. The carbon, helium and other O VI lines can be simultaneously matched by models of this temperature. The O V $\lambda1371.3$ Å is too strong in $T_* = 125\,000$ K models and shows a deep absorption component which is not observed. As we will show below, this line is sensitive to the inclusion of heavier ions in the models and their abundances, and tends to become stronger as new ions are added to the models. Models with a temperature of $200\,000$ K can also be ruled out, since, for the mass-loss rate values that allow reasonable fits of the carbon and helium lines, both O V lines are absent and very strong unobserved Ne VIII features appear in the synthetic spectra, which also show weak O VI lines. The models with the temperatures of $T_* = 150\,000$ and $165\,000$ K better agree with the observed spectra and are shown in Figs 12 and 13, respectively, for different values of the transformed radius. Among the $T_* = 150\,000$ K models, the B150.M70.V2000 one with $\dot{M} = 10^{-7}$ M$_\odot$ yr^{-1} and $R_t = 10.72$ R$_\odot$ fits best all the observed diagnostics, except for the O V $\lambda\lambda2781.0$, 2787.0 Å and $\lambda1371.3$ Å lines, which are only fitted by models of this T_*, by adopting a mass-loss rate twice and 1.3 times higher, respectively. Such a higher mass-loss, however, worsens the fit of all the C IV, He II and O VI lines, except for the O VI $\lambda\lambda1031.9$, 1037.6 Å

doublet, where the intensity of the second component is improved, as shown in Fig. 12. The relative strength of this line, however, is also very sensitive to clumping, since emission lines are affected by it, but not resonance ones (Oskinova, Hamann & Feldmeier 2007), as well as to soft X-rays, and other factors. Among models with the temperature of $T_* = 165\,000$ K, the C165.M65.V2000 one, with a mass-loss rate of $\dot{M} = 10^{-7}$ M$_\odot$ yr^{-1} and a transformed radius of $R_t = 9.03$ R$_\odot$, fits well the observed spectra, again except for the O V lines which are even more discrepant than in the $T_* = 150\,000$ K models, as can be seen in Fig. 13. At any of these two temperatures, the fits of the O V lines require lower values of the transformed radius, which are incompatible with the other diagnostic lines. This effect is worse in the $T_* = 165\,000$ K models than it is in the $T_* = 150\,000$ K ones; from this we conclude that, among the grid models, the B150.M70.V2000 one gives the best fit.

Below, we extend the analysis beyond the model grid comparison and address in depth not only the O V line discrepancy, but also other disagreements between the observations and the best-fitting model, and refine the parameters. We compare the observations with synthetic spectra calculated assuming different values of turbulence velocity, show the effect of different neon, oxygen and argon abundances, put constraints on the nitrogen and iron abundances, and study the impact of adding heavier ions in the synthetic spectra, which are found to affect the ionization fractions of oxygen and improve the O V lines' fit.

5.2 Extending the analysis

In Fig. 11, the O VI $\lambda\lambda1031.9$, 1037.6 Å doublet and the absorption profile of C IV $\lambda\lambda1548.2$, 1550.8 Å are narrower in the $v_\infty = 2000$ km s^{-1} models than in the observations, suggesting that the turbulence velocity in NGC 6905 is higher than that adopted in the calculation of the model grid. Fig. 14 shows that higher values of turbulence velocity, in fact, improve the match of the O VI and C IV profiles.

Another difference between the best-fitting grid model and observed spectra is the absence, in the observed spectra, of N V $\lambda\lambda1238.8$, 1242.8 Å seen in all the models. This is due to a lower nitrogen abundance in this star than we assumed for the grid. Fig. 15 shows models with different nitrogen abundances and $T_* = 150\,000$ K, $\dot{M} = 10^{-7}$ M$_\odot$ yr^{-1} and $v_\infty = 2000$ km s^{-1}. Nitrogen abundances of $X_N < 5.5 \times 10^{-4}$ better match the spectral region shown in Fig. 15, while other spectral lines show no significant differences.
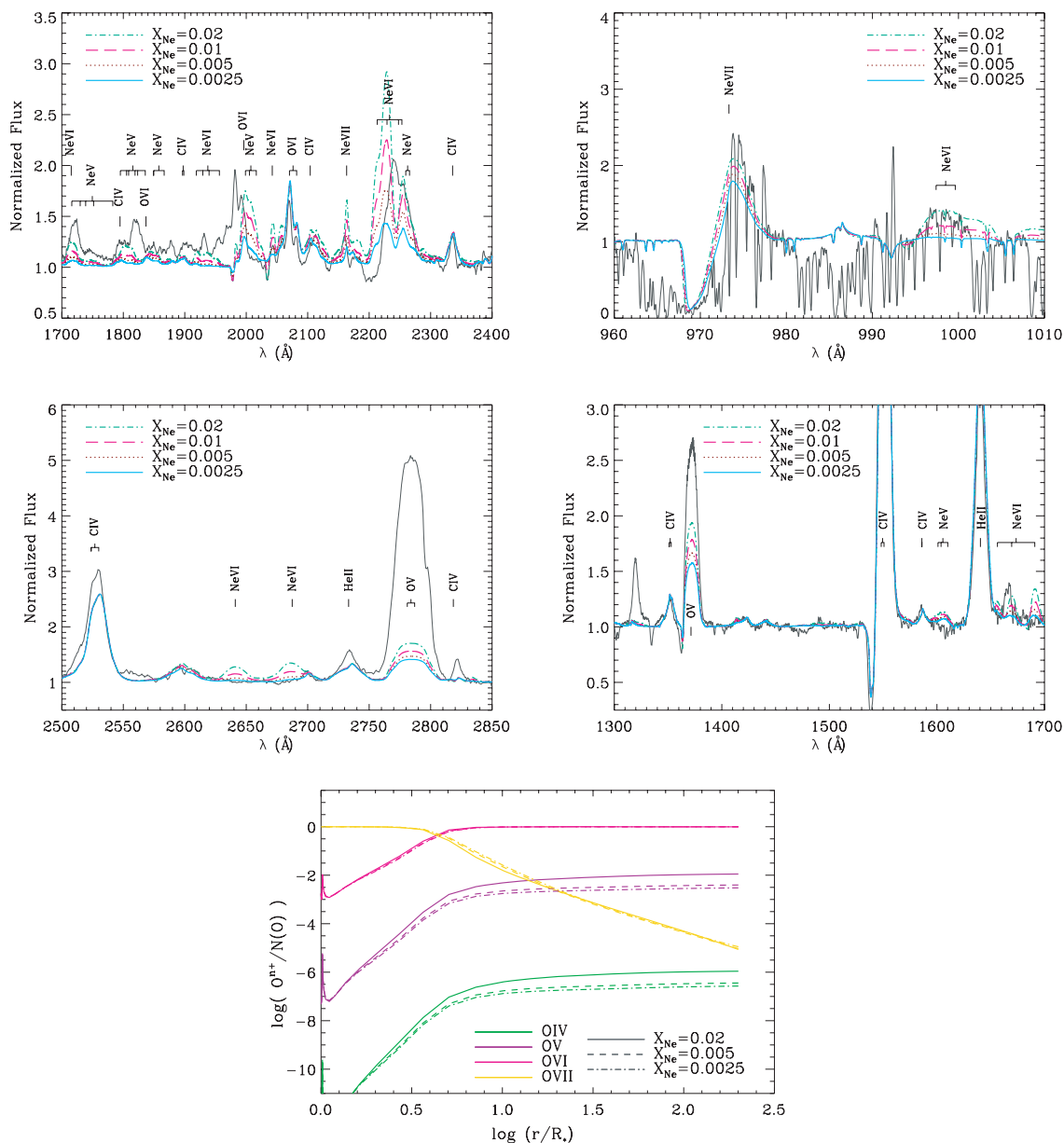
Figure 16. Comparison between NGC 6905 UV and far-UV observed spectra (continuous black line) and models with $T_* = 150$ kK, $\dot{M} = 10^{-7}$ M$_\odot$ yr^{-1}, $v_\infty = 2000$ km s^{-1} and different values of neon abundance. The bottom panel shows the oxygen ion fractions for the different neon abundances.

Several neon features which appear in the synthetic spectra are not observed, indicating that this object may have a lower Ne abundance. Fig. 16 shows models with different neon abundances, and $T_* = 150\,000$ K, $\dot{M} = 10^{-7}$ M$_\odot$ yr^{-1} and $v_\infty = 2000$ km s^{-1}. The neon abundance in the spectra of the central star of NGC 6905 is difficult to constrain due to the lack of strong neon lines other than Ne VII λ973.3 Å and due to the mismatch between Ne VI and Ne V features present in the models in the region 1700–2300 Å and the observations. In Fig. 16, we see that none of the neon abundances adopted improves the fit of the Ne VI complex $\lambda\lambda$2213.1, 2229.1 Å. Also, models with higher neon abundances produce some features which are not seen in the observed spectra such as a Ne VII line at λ2163.4 Å and Ne VI lines at $\lambda\lambda$2641.1, 2687.4 Å. On the other hand, the lower neon abundances produce very weak Ne VII λ973.3 Å and Ne VI $\lambda\lambda$997.4, 999.6 Å lines. The fact that some diagnostics are improved by a higher neon content while others are worsened seems

to point to an incorrect temperature. We did not use the neon lines as a temperature diagnostic as they are, also in the $T_* = 165\,000$ K models, incompatible with other diagnostics. However, we have observed (not shown here) that models with a temperature of $T_* = 200\,000$ K better reproduce several of the neon structures that are incompatible in cooler models. We consider the present analysis inconclusive regarding the neon abundance. An interesting outcome of the comparison between models with different neon abundances is a slight enhancement of the O V λ1371.3 Å and $\lambda\lambda$2781.0, 2787.0 Å lines as the neon content in the models increases, which is the result of an increase in the relative fraction of the O V ion, as can be seen in the bottom panel of Fig. 16.

In an attempt to reproduce the strong O V lines simultaneously with the other diagnostics, we investigated the effect of higher oxygen abundances, which is shown in Fig. 17. For the grid models, we assumed an oxygen mass fraction of $X_O = 0.08$. A higher oxygen

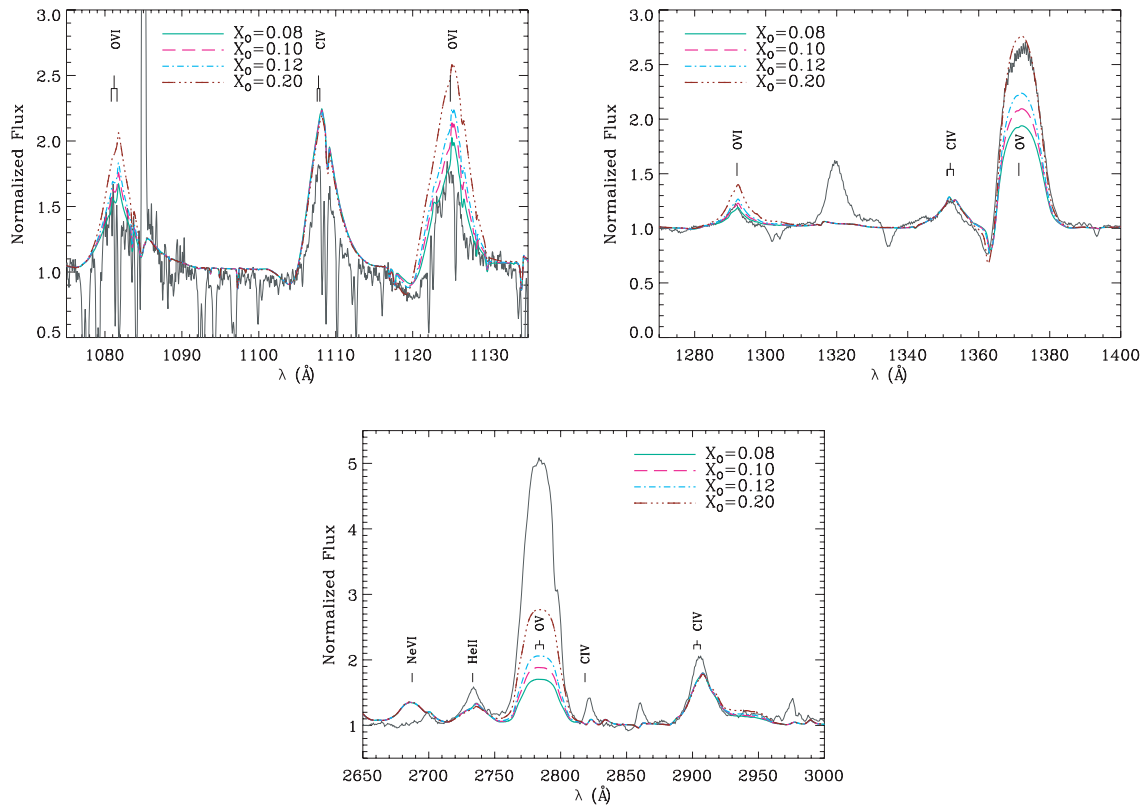**Figure 17.** Observed spectra of the central star of NGC 6905 (continuous black line) and models with $T_* = 150$ kK, $\dot{M} = 10^{-7}$ M$_\odot$ yr^{-1}, $v_\infty = 2000$ km s^{-1} and different values of oxygen abundance. The oxygen mass fraction adopted for the grid models is $X_O = 0.08$.
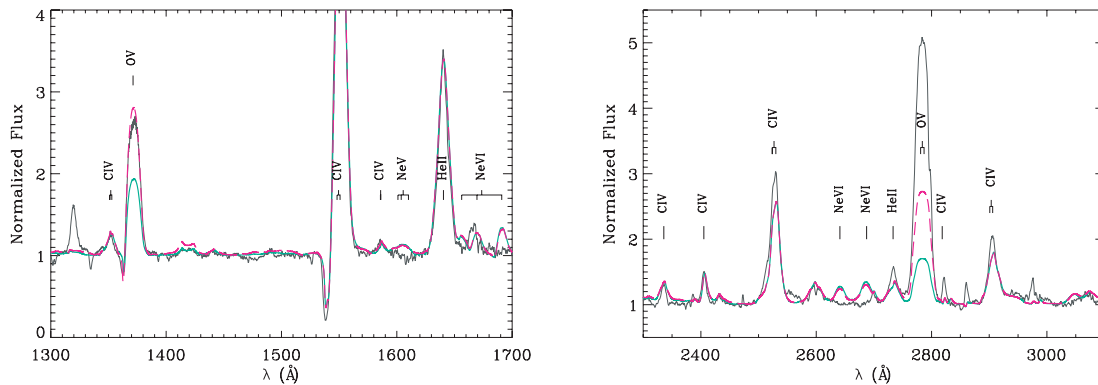

Figure 18. The effect on the synthetic spectra of including new ions in the calculation is seen almost exclusively in the profiles of the O v lines. The observed spectra are shown as a continuous black line. The pink/dashed and green/continuous lines show models with and without the inclusion of new ions, respectively. The models have $T_* = 150$ kK, $\dot{M} = 10^{-7}$ M$_\odot$ yr^{-1} and $v_\infty = 2000$ km s^{-1}.

abundance increases the intensity of the O v lines in the synthetic spectra, but worsens the fit of most of the O vi lines. Besides, even an oxygen mass fraction of $X_O = 0.20$ is not enough to reproduce the strong observed O v $\lambda\lambda 2781.0$, 2787.0 Å line. The O vi $\lambda\lambda 1031.9$, 1037.6 Å doublet does not show any significant change from the increase in the oxygen abundance.

Because of the effect seen in the O v lines due to an increase in neon abundance, we also experimented with the inclusion of new ions in the models in an attempt to reproduce the O v lines' observed intensities. A very complete model including Ni vii, Ni viii, Ni ix, Co vii, Co viii, Co ix, Ca vi, Ca vii, Ca viii, Ca ix, Ca x, Ar vi, Ar vii, Ar viii, Si v, Si vi, Mg v, Mg vi, Mg vii, Na vi, Na vii, Na viii and Na ix in addition to the ions already present in the previous

model was calculated, assuming solar abundances for all the additional elements. As a result, the intensity of the O v $\lambda 1371.3$ Å and $\lambda\lambda 2781.0$, 2787.0 Å lines in the synthetic spectra increased as shown in Fig. 18, while other major features which we used to constrain stellar parameters were unaffected. This is a result of the increase in the O v ion fraction. In particular, the magnesium ions followed by the sodium ones produce most of the effect, while the cobalt and nickel ions cause smaller, but notable, changes in the O v line strengths. The rest of the spectra show minor differences, mainly due to calcium and argon lines.

We further explore this model by altering the abundances considered for some elements and show the effect on the spectra of different abundances of the elements argon and iron. Fig. 19 shows
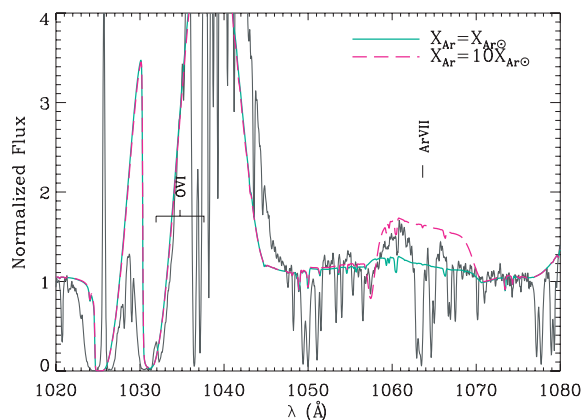
Figure 19. Ar VII λ1063.55 Å in models with different argon abundances. Both models shown have $T_* = 150$ kK, $\dot{M} = 10^{-7}$ M$_\odot$ yr^{-1} and $v_\infty = 2000$ km s^{-1}. The observed spectrum of NGC 6905 is shown as a continuous black line.

Figure 21. The Lyα interstellar absorption in the spectrum of NGC 6905 (continuous black line) is compared with our best-fitting model shown with the effect of different values of the neutral hydrogen column density.

the Ar VII λ1063.55 Å line. This line was first identified as a photospheric absorption by Werner, Rauch & Kruk (2007) in CSPNe and WDs, for which they found roughly solar abundances, in line with nucleosynthesis calculations for AGB stars. We find a model with 10 times the solar abundance to better reproduce the observed feature in this spectral region, confirming the results of Herald & Bianchi (2009) who identified the same line in the *FUSE* spectra of some of the hottest [WC] CSPNe. Fig. 20 shows the effects of different iron abundances in the synthetic spectra. In a recent work, Werner et al. (2010) identified Fe x λλ979.3, 1022.9 Å lines in the *FUSE* spectra of the hot PG1159 stars RX J2117.1+3412, K 116, Longmore 4, NGC 246 and H1504+65, finding a solar iron abundance for these stars. In NGC 6905, we find that iron abundances higher than 0.3 times the solar one produce some unobserved features, especially an absorption on the Ne VII λ973.3 Å P Cygni profile, and can be ruled out.

5.2.1 Interstellar absorption

Figs 21 and 22 show our best-fitting model, which includes the additional heavy ions and an argon abundance of 10 times the solar value, calculated adopting a turbulence velocity $v_{turb} = 150$ km s^{-1}. We applied the interstellar absorption due to atomic and molecular hydrogen, treated as described in Herald & Bianchi (2002, 2004a,b),
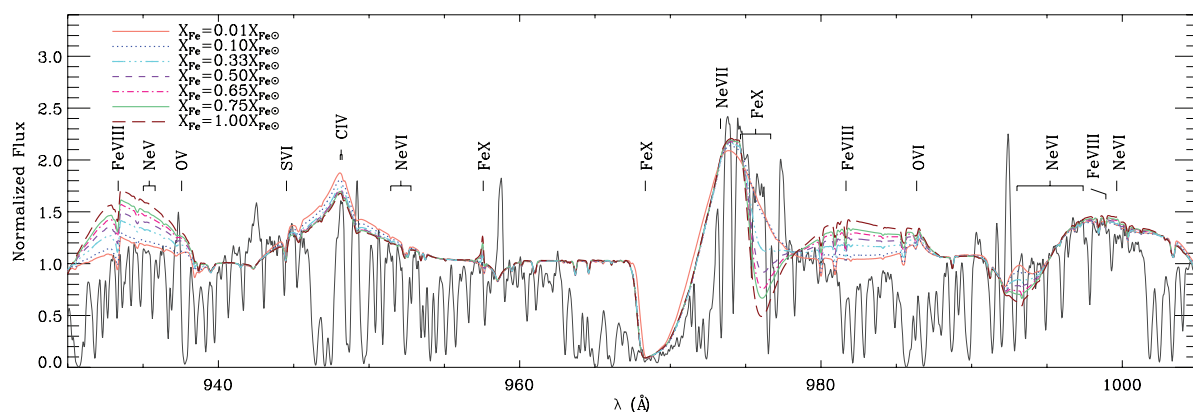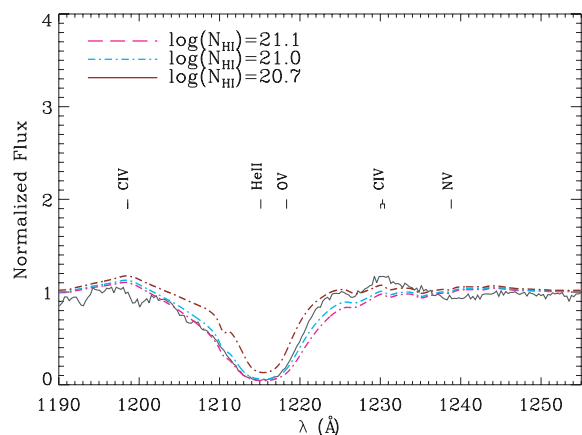
to the synthetic spectra. We assumed that the temperature of the interstellar gas is 100 K, a typical value for the ISM. From fitting the Lyα λ1215 Å H I absorption profile, we derived a neutral hydrogen column density of $20.7 < \log N(\text{H I}) < 21.1$ (where N is given in units of cm^{-2}). Using the numerous H$_2$ absorption lines in the *FUSE* range, we constrained the molecular hydrogen column density to $19.3 < \log N(\text{H}_2) < 19.7$ (where N is given in units of cm^{-2}).

After the stellar parameters have been constrained based on line diagnostics, the observed slope of the spectra was compared to the best-fitting model reddened using different values of the colour excess, as shown in Fig. 23. The reddening of Cardelli, Clayton & Mathis (1989) with $R_V = 3.1$ was adopted. The STIS *G140L* and *G230L* spectral regions are well matched using a colour excess of $E(B - V) = 0.17$ mag, while a lower reddening is required in order to fit the *FUSE* region. Thus, we conclude on a colour excess of $E(B - V) = 0.17 \pm 0.05$ mag. The continuum comparison suggests that the interstellar extinction may be less steep in the UV than the extinction curve adopted. Model continuum accuracy has not yet been reportedly tested versus observations and may be addressed with future work on an expanded sample.

According to Bohlin, Savage & Drake (1978), the neutral hydrogen column density and the colour excess relate as $\langle N(\text{H I})/E(B - V) \rangle = 4.8 \times 10^{21}$ atoms cm^{-2} mag^{-1}. An $E(B - V) = 0.17$ mag implies $\log N(\text{H I}) = 20.9$ (where N is given in units

Figure 20. The observed spectrum of the central star of NGC 6905 (continuous black line) is compared with synthetic spectra for different iron abundances. The models have $T_* = 150$ kK, $\dot{M} = 10^{-7}$ M$_\odot$ yr^{-1} and $v_\infty = 2000$ km s^{-1}. The numerous narrow absorptions are from interstellar H$_2$.
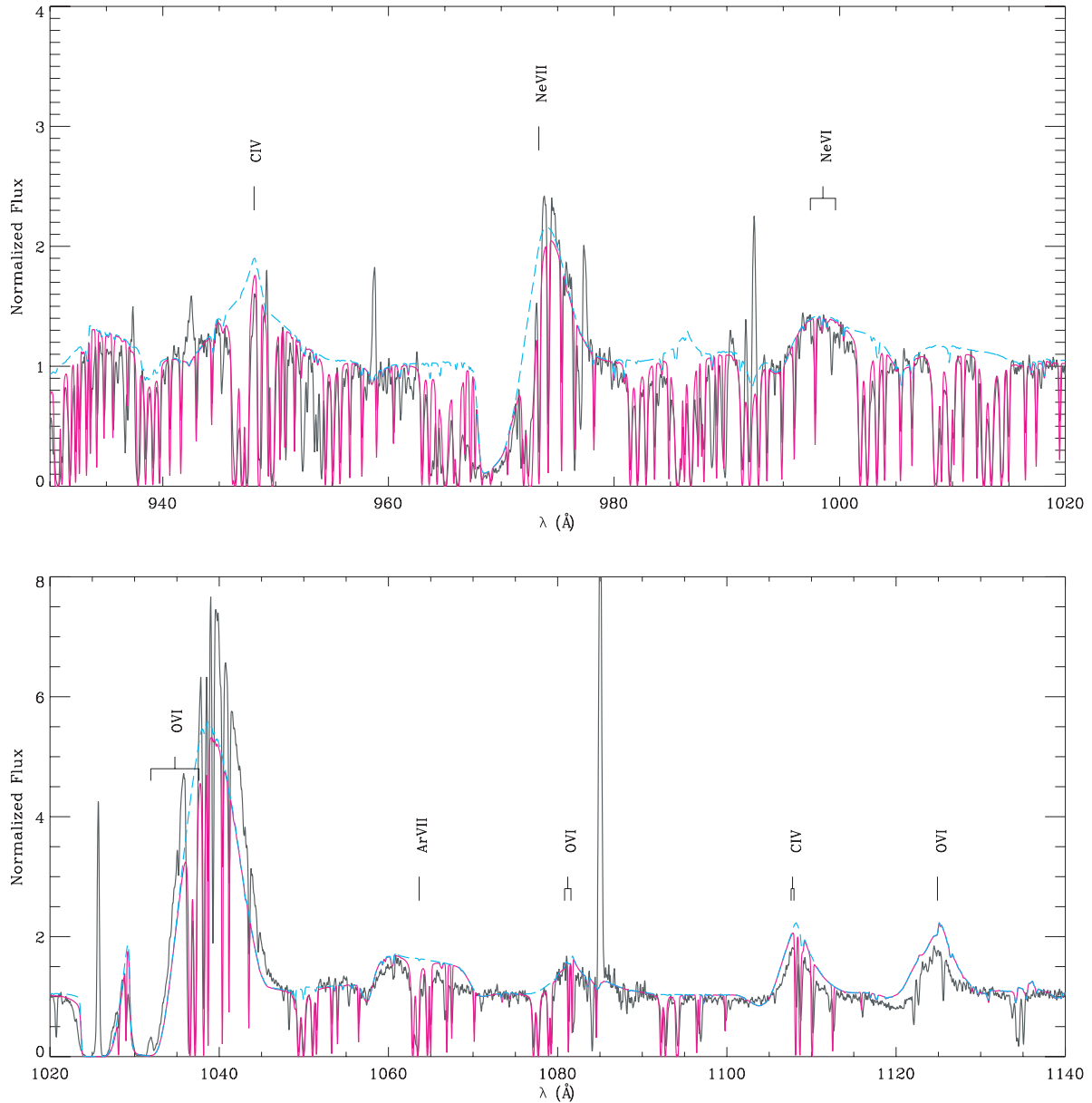
Figure 22. The light-blue dashed line is our best-fitting model. In pink, we apply to this model the effect of the absorption by interstellar molecular hydrogen with a column density of $\log N(\mathrm{H_2}) = 19.5$ (where N is given in units of $\mathrm{cm^{-2}}$). NGC 6905's far-UV observed spectrum is shown as a continuous black line.

of $\mathrm{cm^{-2}}$), which is within the range derived by us from the Lyα $\lambda 1215$ Å absorption.

5.2.2 Results from the analysis

The parameters of our best-fitting grid model are $T_* = 150\,000$ K, $\dot{M} = 1 \times 10^{-7}$ $\mathrm{M_\odot}$ $\mathrm{yr^{-1}}$, $R_\mathrm{t} = 10.7$ $\mathrm{R_\odot}$, $R_* = 0.12$ $\mathrm{R_\odot}$ and $v_\infty = 2000$ $\mathrm{km\,s^{-1}}$. The value of the stellar radius follows the evolutionary track of Miller Bertolami & Althaus (2006) for 0.6-$\mathrm{M_\odot}$ CSPNe and a temperature of 150 000 K. Nevertheless, as discussed previously, two models sharing R_t, v_∞ and T_*, but with different values of R_* and $\dot{M}$ will have similar spectral features. As a consequence, different combinations of parameters result in equally good fits to the observations. In the literature, the distances derived range between 1.7 and 2.6 kpc (Maciel 1984; Cahn, Kaler & Stanghellini

1992; van de Steene & Zijlstra 1994; Zhang 1995; Stanghellini, Shaw & Villaver 2008). If we adopt the most recent and also lower value for the distance, a radius of $R_* = 0.09$ $\mathrm{R_\odot}$ is obtained. A model with this radius and $T_* = 150\,000$ K would be in a lower mass evolutionary track (Miller Bertolami & Althaus 2006) of 0.57 $\mathrm{M_\odot}$, as seen in Fig. 24, where the filled circle is the grid model calculated by us and the open circle is assuming the literature distance of 1.7 kpc. By keeping the transformed radius constant, the radius of $R_* = 0.09$ $\mathrm{R_\odot}$ implies a mass-loss rate of $\dot{M} = 6.2 \times 10^{-8}$ $\mathrm{M_\odot}$ $\mathrm{yr^{-1}}$.

The central star of NGC 6905 has been previously studied in the literature through spectral analyses in optical, UV and far-UV regimes. It has been recently analysed by Marcolino et al. (2007), using low-resolution optical spectra, low-resolution *IUE* spectra and *FUSE* spectra in the 1000–1175 Å interval, which excluded the Ne VII $\lambda 973.3$ Å line from the analysis. They also made use
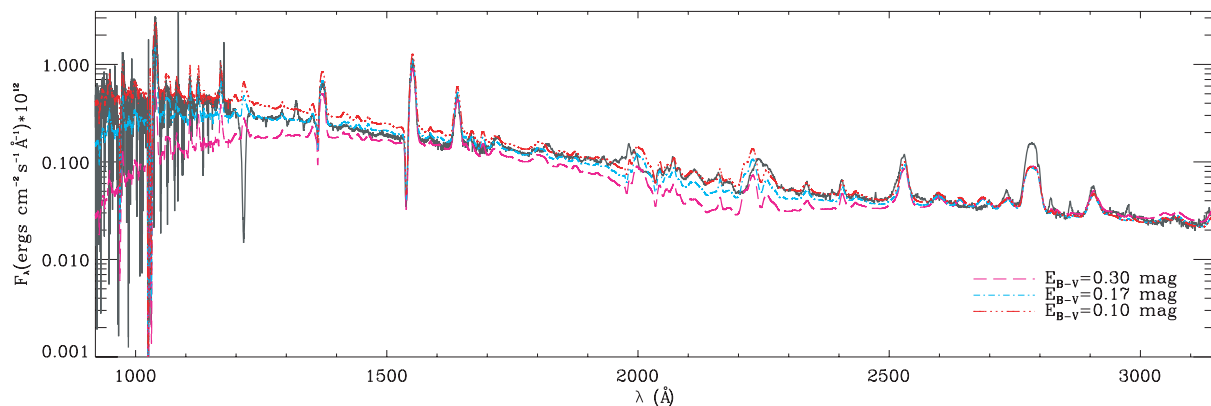
Figure 23. NGC 6905's spectra (continuous black line) along with our best-fitting model reddened with different values of colour excess, assuming Milky Way type extinction with $R_V = 3.1$.
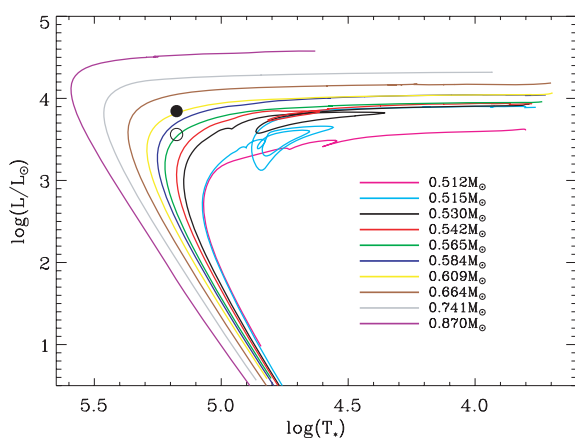

Figure 24. HRD showing the evolutionary tracks of Miller Bertolami & Althaus (2006) and the positions of our best-fitting grid model to NGC 6905 (which would imply a distance of 2.3 kpc), as a filled circle, and of the model rescaled assuming a distance of 1.7 kpc, as an open circle.

of the code CMFGEN to perform the spectral analysis and found parameters close to the values determined by us: $T_* \sim 150\,000$ K, $\dot{M} \sim 7 \times 10^{-8}$ M$_\odot$ yr^{-1}, $R_t = 10.5$ R$_\odot$ and $v_\infty = 1890$ km s^{-1}, considering a clumping filling factor of $f = 0.1$, the same value as adopted by us. In our analysis, we included many ionic species not considered in theirs, which allowed us to achieve a good fit of the O v $\lambda 1371.3$ Å line and improve the fit of the O v $\lambda\lambda 2781.0$, 2787.0 Å line. This example proves the usefulness of the grid for constraining the main stellar parameters and our extended analysis resolved the so-far-inconsistent diagnostic of the O v lines.

6 SUMMARY AND CONCLUSIONS

We have used the state-of-the-art stellar atmosphere code CMFGEN to build a comprehensive grid of synthetic spectra covering the range of stellar parameters appropriate for H-deficient CSPNe of temperatures above 50 000 K. The models account for line blanketing, non-LTE expanding atmospheres (where the velocity law is fixed and the mass-loss rate is a free parameter) and wind clumping. Many ionic species neglected in previous models were included (Table 4). We provide a uniform set of models that allows systematic analysis of far-UV, UV, optical and IR observed spectra in order to constrain photospheric and wind parameters. We examined the far-UV, UV and optical synthetic spectra of the grid and selected spectral fea-

tures best suited for constraining values of the mass-loss rate and stellar temperature.

We also analysed the effect of soft X-rays on the synthetic spectra. We found that, at $T_* = 165\,000$ K, an unlikely high X-ray luminosity is necessary in order to cause a relevant effect in the spectra. At $T_* = 100\,000$ K, a reasonable value of L_X strongly affects the O VI $\lambda\lambda 1031.9$, 1037.6 Å line. For the $T_* = 65\,000$ K model, an even lower value of X-ray luminosity is sufficient to affect the O VI doublet.

As a sample application of the grid, we used it to analyse the UV spectra of the central star of NGC 6905, showing that the grid can be used to constrain the photospheric and wind parameters to a good extent and to greatly facilitate more detailed analysis.

For NGC 6905, the temperature of our best-fitting model is also a lower limit, since any lower temperature model would produce a too strong O v $\lambda 1371.3$ Å line which, as we have shown, is also affected by the inclusion of new ions. A slightly higher temperature for this star improves the fits of the far-UV O VI doublet and Ne VII line, while the other diagnostics remain acceptable. Thus, we constrain the temperature of the central star of NGC 6905 as being between 150 000 and 165 000 K, an overall uncertainty of 10 per cent.

We extended the study beyond the grid of models by considering parameters that were not explored in the grid. We found higher values of the turbulence velocity to improve the fit of O VI $\lambda\lambda 1031.9$, 1037.6 Å and C IV $\lambda\lambda 1548.2$, 1550.8 Å lines. We showed the effects of different abundances of neon, oxygen and argon, and we were able to put constraints on the nitrogen and iron abundances, both subsolar. In this object, a lower value of nitrogen abundance than the one chosen for the grid was necessary to fit the observed spectra. For all plausible temperatures, we were unable to adequately fit all neon diagnostics simultaneously with a single neon abundance.

By adding heavier ions to the best-fitting grid model, we were able, for the first time, to reproduce the observed intensity of the O v $\lambda 1371.3$ Å line and to improve the fit of the O v $\lambda\lambda 2781.0$, 2787.0 Å line. Finally, by fitting the several H$_2$ absorption lines present in the *FUSE* range and the Lyα absorption profile, we constrained the molecular and neutral hydrogen column densities and, by comparing the slope of the observed spectra to our best-fitting model, we derived the colour excess, which is in agreement with the value expected from the H I column density measured.

The grid of synthetic spectra presented here is available online at http://dolomiti.pha.jhu.edu/planetarynebulae.html. Additional models will be added to the grid in the future, covering the temperature regime below 50 000 K, as well as new grids for

different surface gravity regimes, suitable for the study of PG1159 stars that present wind signatures in their spectrum.

ACKNOWLEDGMENTS

REFERENCES

Bianchi L., 2009, Ap&SS, 320, 11
Bianchi L., Garcia M., 2002, ApJ, 581, 610
Bianchi L., Herald J., 2007, in Gómez de Castro A. I., Barstow M. A., eds, Proc. of the Joint Disc. n.4 during the IAU gen. Assem. of 2006. UV Astronomy: Stars from Birth to Death. ISBN 978-84-7491-852-6, p. 89
Bianchi L. et al., 2005, ApJ, 619, L27
Bianchi L., Herald J. E., Garcia M., 2007a, in Gómez de Castro A. I., Barstow M. A., eds, Proc. of the Joint Disc. n. 4 during the IAU gen. Assem. of 2006. UV Astronomy: Stars from Birth to Death. ISBN 978-84-7491-852-6, p. 101
Bianchi L. et al., 2007b, ApJS, 173, 659
Bianchi L., Herald J., Garcia M., 2009, in van Steenberg M. E., Sonneborn G., Moos H. W., Blair W. P., eds, AIP Conf. Ser. Vol. 1135, Future Directions in Ultraviolet Spectroscopy. Am. Inst. Phys., New York, p. 145
Bianchi L., Efremova B., Herald J., Girardi L., Zabot A., Marigo P., Martin C., 2011a, MNRAS, 411, 2770
Bianchi L., Herald J. E., Efremova B., Girardi L., Zabot A., Marigo P., Conti A., Shiao B., 2011b, in Shustov B., Gómez de Castro A. I., Sachkov M., eds, APSS Special Issue. The UV Universe 2010. In press (doi:10.1007/s10509-010-0581-x)
Blöcker T., 2001, Ap&SS, 275, 1
Bohlin R. C., Savage B. D., Drake J. F., 1978, ApJ, 224, 132
Cahn J. H., Kaler J. B., Stanghellini L., 1992, A&AS, 94, 399
Cardelli J. A., Clayton G. C., Mathis J. S., 1989, ApJ, 345, 245
Chlebowski T., Garmany C. D., 1991, ApJ, 368, 241
Chlebowski T., Harnden F. R. Jr, Sciortino S., 1989, ApJ, 341, 427
Clegg R. E. S., Middlemass D., 1987, MNRAS, 228, 759
Crowther P. A., Abbott J. B., Hillier D. J., De Marco O., 2003, in Kwok S., Dopita M., Sutherland R., eds, Proc. IAU Symp. 209, Planetary Nebulae: Their Evolution and Role in the Universe. Astron. Soc. Pac., San Francisco, p. 243
De Marco O., Crowther P. A., Barlow M. J., Clayton G. C., de Koter A., 2001, MNRAS, 328, 527
Evans N. R., Seward F. D., Krauss M. I., Isobe T., Nichols J., Schlegel E. M., Wolk S. J., 2003, ApJ, 589, 509
Garcia M., Bianchi L., 2004, ApJ, 606, 497
Górny S. K., Tylenda R., 2000, A&A, 362, 1008
Grosdidier Y., Acker A., Moffat A. F. J., 2000, A&A, 364, 597
Grosdidier Y., Acker A., Moffat A. F. J., 2001, A&A, 370, 513
Guerrero M. A., Chu Y.-H., Gruendl R. A., Williams R. M., Kaler J. B., 2001, ApJ, 553, L55
Hamann W.-R., Gräfener G., 2004, A&A, 427, 697
Hamann W.-R., Koesterke L., Wessolowski U., 1993, A&A, 274, 397
Herald J. E., Bianchi L., 2002, ApJ, 580, 434
Herald J. E., Bianchi L., 2004a, ApJ, 609, 378
Herald J. E., Bianchi L., 2004b, ApJ, 611, 294
Herald J., Bianchi L., 2009, in van Steenberg M. E., Sonneborn G., Moos H. W., Blair W. P., eds, AIP Conf. Ser. Vol. 1135, Future Directions in Ultraviolet Spectroscopy. Am. Inst. Phys., New York, p. 151
Herald J. E., Bianchi L., Hillier D. J., 2005, ApJ, 627, 424

Herwig F., 2001, Ap&SS, 275, 15
Herwig F., 2005, ARA&A, 43, 435
Herwig F., Lugaro M., Werner K., 2003, in Kwok S., Dopita M., Sutherland R., eds, Proc. IAU Symp. 209, Planetary Nebulae: Their Evolution and Role in the Universe. Astron. Soc. Pac., San Francisco, p. 85
Hillier D. J., Lanz T., 2001, in Ferland G., Savin D. W., eds, ASP Conf. Ser. Vol. 247, Spectroscopic Challenges of Photoionized Plasmas. Astron. Soc. Pac., San Francisco, p. 343
Hillier D. J., Miller D. L., 1998, ApJ, 496, 407
Hillier D. J., Lanz T., Heap S. R., Hubeny I., Smith L. J., Evans C. J., Lennon D. J., Bouret J. C., 2003, ApJ, 588, 1039
Hubeny I., Lanz T., 1995, ApJ, 439, 875
Iben I. Jr, Kaler J. B., Truran J. W., Renzini A., 1983, ApJ, 264, 605
Karakas A. I., 2010, MNRAS, 403, 1413
Koesterke L., Hamann W.-R., 1997a, in Habing H. J., Lamers H. J. G. L. M., eds, Proc. IAU Symp. 180, Planetary Nebulae. Kluwer, Dordrecht, p. 114
Koesterke L., Hamann W.-R., 1997b, A&A, 320, 91
Koesterke L., Dreizler S., Rauch T., 1998, A&A, 330, 1041
Kurucz R. L., 1991, Stellar Atmospheres: Beyond Classical Models. Reidel, Dordrecht
Lamers H. J. G. L. M., Cassinelli J. P., 1999, Introduction to Stellar Winds. Cambridge Univ. Press, Cambridge
Lanz T., Hubeny I., 2003, ApJS, 146, 417
Lanz T., Hubeny I., 2007, ApJS, 169, 83
Leuenhagen U., Hamann W.-R., 1998, A&A, 330, 265
Leuenhagen U., Hamann W.-R., Jeffery C. S., 1996, A&A, 312, 167
Lucy L. B., White R. L., 1980, ApJ, 241, 300
Maciel W. J., 1984, A&AS, 55, 253
Marcolino W. L. F., Hillier D. J., de Araujo F. X., Pereira C. B., 2007, ApJ, 654, 1068
Marigo P., 2001, A&A, 370, 194
Martin D. C. et al., 2005, ApJ, 619, L1
Martins F., Schaerer D., Hillier D. J., Meynadier F., Heydari-Malayeri M., Walborn N. R., 2005, A&A, 441, 735
Miller Bertolami M. M., Althaus L. G., 2006, A&A, 454, 845
Moffat A. F. J., 2008, in Hamann W.-R., Feldmeier A., Oskinova L. M., eds, Proc. of an Int. Workshop held in Potsdam, Ger., 18–22 June 2007, Clumping in Hot-Star Winds. Universitatsverlag, Potsdam, p. 17
Oskinova L. M., Hamann W.-R., Feldmeier A., 2007, A&A, 476, 1331
Owocki S. P., Castor J. I., Rybicki G. B., 1988, ApJ, 335, 914
Pauldrach A., Puls J., Kudritzki R. P., Mendez R. H., Heap S. R., 1988, A&A, 207, 123
Pauldrach A. W. A., Hoffmann T. L., Lennon M., 2001, A&A, 375, 161
Peña M., Stasińska G., Medina S., 2001, A&A, 367, 983
Rauch T., 2003, A&A, 403, 709
Raymond J. C., Smith B. W., 1977, ApJS, 35, 419
Schmutz W., Hamann W.-R., Wessolowski U., 1989, A&A, 210, 236
Stanghellini L., Shaw R. A., Villaver E., 2008, ApJ, 689, 194
Stasińska G., Gräfener G., Peña M., Hamann W.-R., Koesterke L., Szczerba R., 2004, A&A, 413, 329
Todt H., Hamann W.-R., Gräfener G., 2008, in Hamann W.-R., Feldmeier A., Oskinova L. M., eds, Proc. of an Int. Workshop held in Potsdam, Ger., 18–22 June 2007. Clumping in Hot-Star Winds. Universitatsverlag, Potsdam, P. 251
van de Steene G. C., Zijlstra A. A., 1994, A&AS, 108, 485
Vassiliadis E., Wood P. R., 1994, ApJS, 92, 125
Werner K., 2001, Ap&SS, 275, 27
Werner K., Heber U., 1991, A&A, 247, 476
Werner K., Herwig F., 2006, PASP, 118, 183
Werner K., Jahn D., Rauch T., Reiff E., Herwig F., Kruk J. W., 2006, Mem. Soc. Astron. Ital., 77, 996
Werner K., Rauch T., Kruk J. W., 2007, A&A, 466, 317
Werner K., Rauch T., Kruk J. W., 2010, ApJ, 719, L32
Zhang C. Y., 1995, ApJS, 98, 659

This paper has been typeset from a TEX/LATEX file prepared by the author.